

Turbulent dynamics of sinusoidal oscillatory flow over a wavy bottom

Asim Önder^{1,†} and Jing Yuan¹

¹Department of Civil and Environmental Engineering, National University of Singapore, Singapore 117576, Singapore

(Received 8 January 2018; revised 18 September 2018; accepted 18 September 2018; first published online 2 November 2018)

A direct numerical simulation study is conducted to investigate sinusoidal oscillatory flow over a two-dimensional wavy wall. The height and wavelength of the bottom profile, and the period and amplitude of the free-stream oscillation, are selected to mimic a wave-driven boundary layer over vortex ripples on a sandy seabed. Two cases with different Reynolds numbers (Re) are considered, and the higher- Re case achieves a fully developed turbulent state with a wide separation between the energy-containing and dissipative scales. The oscillatory flow is characterized by coherent columnar vortices, which are the main transport agents of turbulent kinetic energy and enstrophy. Two classes of coherent vortices are observed: (i) a primary vortex formed at the lee side of the ripple by flow separation at the crest; (ii) a secondary vortex formed beneath the primary vortex by vortex-induced separation. When the free-stream velocity weakens, these vortices form a counter-rotating vortex dipole and eject themselves over the crest with their mutual induction. Turbulence production peaks twice in a half-cycle; during the formation of the primary vortex and during the ejection of the vortex dipole. The intensity of the former peak remains low in the lower- Re case, as the vortex dipole follows a higher altitude trajectory limiting its interactions with the bottom, and leaving minimal residual turbulence around the ripples for the subsequent half-cycle. Flow snapshots and spectral analysis reveal two dominant three-dimensional features: (i) an energetic vortex mode with a preferred spanwise wavelength close to the ripple wavelength; (ii) streamwise vortical structures in near-wall regions with a relatively shorter spanwise spacing influenced by viscous effects. The vortex mode becomes strong when the cores of the vortices are strained to an elliptical form while moving towards the crest. Following the detachment of the vortices from the ripple, the vortex mode in the higher- Re case breaks down the spanwise coherence of the columnar vortices and decomposes them into intermittent patches of turbulent vortex clusters. The distribution of wall shear stress over the ripple is also analysed in detail. The peak values are observed near the ripple crest around the ejection of the vortex dipole and the maximum free-stream velocity. In the former, both the vortex mode and streamwise vortices have strong footprints on the wall, yielding a bimodal wall-shear-stress spectrum with two distinctive peaks. In the second high-stress regime, decaying coherent vortices impose strong inhomogeneity on the wall shear stress as their wall-attached parts sweep the ripples. These spanwise

† Email address for correspondence: asim.onder@gmail.com

variations in the wall shear provide insights into the instability of two-dimensional sand ripples.

Key words: coastal engineering, separated flows, vortex flows

1. Introduction

Sinusoidal oscillatory flow over two-dimensional wavy bedforms represents an idealized model for wave-induced flow over a ripple-covered seabed, a ubiquitous configuration in coastal regions. This oscillatory flow is significantly different than the flow over flat beds due to the presence of large-scale spanwise vortices. These coherent vortices are formed during each half-cycle by flow separation at ripple crests (Darwin 1883; Bagnold & Taylor 1946). While forming, the adverse gradients in their pressure fields give rise to secondary vortices on the ripple surface (Blondeaux & Vittori 1991, 1999). The resulting vortex pairs are eventually washed over the ripple crests and ejected into the free stream during the flow reversal (Nakato *et al.* 1977). In this phase, the vortices can suspend considerable amounts of sediments, cf. e.g. Honji, Kaneko & Matsunaga (1980), van der Werf *et al.* (2006) and van der Werf *et al.* (2007). Due to this prominence of vortices in the local hydrodynamics, sand ripples are usually referred to as vortex ripples (Nielsen 1992). Natural vortex ripples have wavelengths of $O(10\text{ cm})$ (Mei & Liu 1993), and the vortex formation and ejection events occur in fully turbulent regimes. To date, the dynamics of the flow in these regimes is not sufficiently explored in detail. This work is an effort in this direction. We perform direct numerical simulations (DNS) of sinusoidal oscillatory flow over a periodic array of two-dimensional ripples.

1.1. General properties of vortex ripples

For a specific ripple profile, the oscillatory flow around it has three essential length scales: the wave-orbital amplitude A , the ripple wavelength λ , the ripple height η ; and a time scale: the wave period T , which is used to define the angular frequency $\omega = 2\pi/T$. These characteristic length and time scales, together with the fluid kinematic viscosity ν , are conveniently merged into three dimensionless parameters: Reynolds number

$$Re = \frac{A^2\omega}{\nu}, \quad (1.1)$$

(typically in the range $O(10^4\text{--}10^5)$), Keulegan–Carpenter number

$$K_C = 2\pi \frac{A}{\lambda}, \quad (1.2)$$

giving the ratio of the ambient excursion amplitude to the ripple wavelength (typically in the range $O(1\text{--}10)$) and ripple steepness

$$s = \frac{\eta}{\lambda}, \quad (1.3)$$

with typical values between 0.1 and 0.2.

Study	Facility	$Re = A^2\omega/\nu$	$K_C = 2\pi A/\lambda$	$s = \eta/\lambda$
Sato <i>et al.</i> (1985)	OWT	9100–93 500	4–12.7	0.1
Earnshaw & Greated (1998)	towing tank	23 000–116 000	5–11.3	0.16
Fredsøe <i>et al.</i> (1999)	wave flume	23 000	2.75	0.16
Ourmieres & Chaplin (2004)	wave flume	$\leq 15 000$	0.94–6.28	0.05–0.175
Jespersen <i>et al.</i> (2004)	oscillating lid	2200, 7500	(3.14–5.78) ^a	single ripple
Blondeaux, Scandura & Vittori (2004)	DNS	1250–1600	4.7	0.125–0.15
Nichols & Foster (2007)	wave flume	$\leq 600 000$	45.6	0.1
Canals & Pawlak (2011)	oscillating lid	700–7500	(0.2–2) ^a	single ripple
Hare <i>et al.</i> (2014)	oscillatory tray	160 000	12.5	0.18

TABLE 1. Summary of previous studies on oscillatory flow over vortex ripples. OWT stands for oscillatory water tunnel.

^aIn experiments with a single ripple, the K_C number is calculated using the ripple height, i.e. $K_C = 2\pi A/\eta$.

A considerable amount of knowledge on the turbulent flow over vortex ripples has been obtained from laboratory experiments with rigid ripple models or sand ripples under equilibrium conditions. Table 1 presents a short bibliographical list of previous works. Sato, Mimura & Watanabe (1985) were among the first to explore how the turbulence production and hydrodynamic forces are related to the dynamics of coherent lee vortices. Earnshaw & Greated (1998) and Jespersen *et al.* (2004) characterized the oscillatory flow over rigid ripples using vorticity dynamics. To this end, they calculated the circulation, area and trajectory of the lee vortices. Fredsøe, Andersen & Sumer (1999) visualized the formation and ejection sequence of the primary lee vortex, and showed that the intensity of turbulence near the ripple surface increases substantially when the lee vortex is washed over the crest. Nichols & Foster (2007) studied movable sand ripples under large-scale free-surface wave conditions. They showed that the intensity of instantaneous vortical structures is correlated with the K_C number. Hare *et al.* (2014) investigated the spatial and temporal structures of the flow over sand ripples with turbulence-resolving experiments. Besides the basic first-order flow statistics, they measured the distribution of Reynolds stresses, and the turbulent kinetic energy and its production rate.

Due to resolution restrictions, the experimental measurements did not address more detailed characteristics such as the distribution of wall shear stresses over the ripple surface. These properties were predicted using large-eddy simulations (LES), e.g. Zedler & Street (2006) and Grigoriadis, Dimas & Balaras (2012). However, the subgrid-scale and wall models in these simulations are yet to be verified using DNS or high-resolution experimental data.

1.2. The three-dimensional structure

Despite possible implications for sediment transport and the emergence of three-dimensional ripple patterns under sea waves, the three-dimensional organization and dynamics of the flow over vortex ripples have received relatively little attention. To this end, Ourmieres & Chaplin (2004) studied these features in disturbed laminar

regimes in which the flow exhibits organized structures without breakdown to turbulence. Two types of three-dimensional pattern were reported. The first one was a short-wavelength pattern in the form of equally spaced bridges along the spanwise vortex columns. These structures were driven by centrifugal instabilities. Their spanwise spacing scaled with the inverse of the Taylor number, which quantifies the ratio of centrifugal forces to viscous forces and reads

$$Ta = \frac{A^2 \eta}{2\lambda^2} \sqrt{\frac{\omega}{\nu}} \quad (1.4)$$

in the case of vortex ripples (Hara & Mei 1990). In general, centrifugal instabilities may manifest themselves as azimuthally oriented vortex filaments on the periphery of columnar vortices (Williamson 1996), or streamwise-aligned Görtler vortices in boundary layers around curved walls (Saric 1994; Gschwind, Regele & Kottke 1995). Scandura, Vittori & Blondeaux (2000) observed Görtler vortices over vortex ripples during the first stages of transition into three-dimensionality. Similar streamwise vortex patterns were also reported by Blondeaux *et al.* (2004) in their low Reynolds number DNS simulations (cf. table 1). However, they attributed the phenomena to an inviscid mechanism, which is similar to the production of rib vortices in the braid regions of free-shear flows. In this mechanism, the two-dimensional base flow is subject to some secondary instabilities introducing the initial perturbations which are then continuously stretched to form streamwise vortex pairs in regions with hyperbolic flow topology. This streamwise-vortex production mechanism, i.e. the collapse of perturbed vortex sheets under straining into elongated vortices, was theoretically analysed by Neu (1984) before.

The second pattern reported by Ourmieres & Chaplin (2004) was a brick pattern, which was in the form of shifted bridges of dye between the crests. The brick patterns have spanwise wavelengths in the range $0.6 < \lambda_z/\lambda < 1.3$. The spanwise shifting of the pattern from crest to crest has been observed to be approximately 0.5λ . This long-wavelength pattern has slightly smaller dimensions than the spanwise modes observed in steady boundary layers over wavy walls. For these stationary flows, Günther & Von Rohr (2003) reported a dominant mode at a spanwise spacing of $O(1.5\lambda)$.

Canals & Pawlak (2011) investigated the onset of three-dimensionality in coherent columnar vortex pairs using an oscillating flap – an idealized configuration with similar coherent-vortex dynamics to vortex ripples. They observed structures with spanwise wavelengths in the range $2 < \lambda_z/r < 5$, where r is the vortex-core radius. They associated these structures with elliptic instabilities of vortex cores, as the observed dimensions were in the theoretical range of these instabilities, and a mutually imposed straining was clearly observed in the vortex cores. Canals & Pawlak (2011) further speculated that the initial perturbations feeding the elliptic instabilities were due to centrifugal instabilities.

1.3. The scope of the work

High-fidelity numerical simulations have played an indispensable role in elucidating various turbulence mechanisms in stationary canonical flows, cf. e.g. the recent reviews by Jiménez (2012), Jordan & Colonius (2013), da Silva *et al.* (2014). However, detailed numerical investigations remain limited for non-stationary or oscillatory turbulent flows due to the necessity of long integration times to acquire time-varying statistics. To this end, most progress has been made for oscillatory

boundary layers on flat bottoms thanks to their geometrical simplicity. For these flows, DNS studies in disturbed-laminar regimes helped to characterize the transition mechanisms (Vittori & Verzicco 1998; Mazzuoli, Vittori & Blondeaux 2011; Ozdemir, Hsu & Balachandar 2014; Mazzuoli & Vittori 2016), and the near-wall flow structures in more turbulent regimes were identified using wall-resolved LES (Salon, Armenio & Crise 2007) or DNS (Ghodke & Apte 2016; Scandura, Faraci & Foti 2016). The numerical efforts in the case of vortex ripples have been more modest. The wavy wall breaks the homogeneity in the streamwise direction and prevents statistical averaging over this direction. Consequently, a significantly longer time is required to converge the statistics. This poses an enormous computational challenge at Reynolds numbers close to field conditions, which has not been tackled yet by the community. The present effort is a novel attempt in this regard.

We conduct two DNS cases with $Re = 2500, 10\,000$; $K_C = 5/3\pi \approx 5.24$; and $s = 1/6$ over a periodic array of two-dimensional ripples. The selected ripple profile is slightly steeper than a sinusoidal profile due to presence of a second harmonic. The characteristic coherent spanwise vortices in the high- Re case are in a fully developed post-mixing transition (Dimotakis 2000) regime, where a wide separation between energy- and enstrophy-dominated scales takes place. A primary objective of our work is the detailed analysis of the two-dimensional phase-locked dynamics of coherent spanwise vortices, and their influence on wall-shear-stress distributions. Furthermore, to our knowledge, the three-dimensional features of the flow in fully turbulent regimes have not yet been explored. We will show that the flow exhibits dominant large-scale three-dimensional features even in highly turbulent conditions, and will study the effect of these features on wall-shear-stress fluctuations.

This paper is organized as follows. In §2, we introduce the problem and the numerical methodology, which is a Fourier spectral/hp element method. Then, vortex kinematics over a half-cycle is discussed in §3. Subsequently, §4 analyses the global turbulent kinetic energy budget. Section 5 focuses on turbulent phase-averaged fields, as well as on turbulence statistics along certain representative locations such as vortex cores and turbulence-production peaks. Section 6 analyses the spanwise structure of the flow based using instantaneous snapshots and spectral analysis. Finally, conclusions are given in §7.

2. Problem formulation

This section is devoted to the presentation of the problem and its numerical solution method. The selected flow configuration is presented in §2.1. Subsequently, direct numerical simulation (DNS) with a Fourier spectral/hp finite element method (FEM) is briefly described in §2.2, followed by a discussion of the employed grid resolution in §2.3.

2.1. Flow configuration

We consider a sinusoidally oscillatory viscous flow over a wavy bottom. A Cartesian coordinate system is considered with x, y, z corresponding to streamwise, wall-normal and spanwise directions, respectively. The governing equations are the incompressible Navier–Stokes equations and the continuity equation, which read in the selected coordinate system as follows

$$\frac{\partial u_i}{\partial t} + u_j \frac{\partial u_i}{\partial x_j} = \frac{1}{\rho} \frac{\partial \sigma_{ij}}{\partial x_j} + f_\infty \delta_{ix}, \quad (2.1)$$

Cases	C1	C2
Reynolds number ($Re = A^2\omega/\nu$)	10000	2500
Keulegan–Carpenter number ($K_C = 2\pi A/\lambda$)	5.24	5.24
Ripple slope ($s = \eta/\lambda$)	1/6	1/6
Stokes length to ripple height (δ_s/η)	0.07	0.14
Reynolds number using Stokes length ($Re_\delta = U_0\delta_s/\nu$)	141.42	70.71
Taylor number ($Ta = A^2\eta\sqrt{\omega/\nu}/2\lambda^2$)	3.47	6.94

TABLE 2. Dimensionless parameters for the investigated cases.

$$\frac{\partial u_i}{\partial x_i} = 0, \quad (2.2)$$

where $\mathbf{u} = [u_x, u_y, u_z]$ is the velocity field, $\boldsymbol{\sigma}$ is the stress tensor. For an incompressible Newtonian fluid, the stress tensor is given by $\sigma_{ij} = -p\delta_{ij} + \tau_{ij}$, where p is the pressure field excluding the driving oscillatory pressure p_0 , and $\boldsymbol{\tau}$ is the viscous stress tensor $\tau_{ij} = 2\mu\mathbf{s}_{ij}$ with $\mathbf{s}_{ij} = ((\partial u_i/\partial x_j) + (\partial u_j/\partial x_i))/2$ being the rate of strain tensor. The term f_∞ in (2.1) is the driving uniform oscillatory pressure gradient given by

$$f_\infty = -\frac{1}{\rho} \frac{\partial p_0}{\partial x} = U_0\omega \sin(\omega t), \quad (2.3)$$

which induces a sinusoidal streamwise velocity in the free stream

$$u_0 = -U_0 \cos(\omega t). \quad (2.4)$$

Streamwise, wall-normal and spanwise directions are associated with unit vectors $\hat{\mathbf{i}}, \hat{\mathbf{j}}$ and $\hat{\mathbf{k}}$, respectively. We will simply denote ωt as θ hereafter.

The ripple profile is defined as the superposition of two harmonics

$$y_\eta = \frac{\eta}{2} (\cos \kappa_r x + \eta' \cos 2\kappa_r x), \quad (2.5)$$

where $\kappa_r = 2\pi/\lambda$ is the wavenumber of the waviness with λ being the ripple wavelength, and where η is the ripple height, cf. figure 1. The ratio of ripple height to ripple length is specified to be $\eta/\lambda = 1/6$, and the relative amplitude of the second harmonic is prescribed to be $\eta' = 0.17$. This generic ripple shape is generalized from recent laboratory experiments (Yuan, Dongxu & Madsen 2017), in which sand ripples were produced under sinusoidal oscillatory flows over a coarse-sand (diameter 0.51 mm) movable bed. It should be noted that the flow conditions in the experiments have a higher Re ($\sim O(10^5)$) than that in our simulations. This, however, does not defeat the main objective of this study, which is revealing the fundamental turbulence characteristics for oscillatory flows over vortex ripples using an idealized model.

Two cases with different Reynolds numbers are considered, cf. table 2. Case C1 has a higher Reynolds number with $Re = 10000$. A dimensional instance of this case would be, e.g. $U_0 = 17.77 \text{ cm s}^{-1}$, $T = 2 \text{ s}$, $\nu = 10^{-6} \text{ m}^2 \text{ s}^{-1}$, $\lambda = 6.78 \text{ cm}$ and $\eta = 1.13 \text{ cm}$, which is close to the vortex ripples generated in some laboratory wave flumes (e.g. Nichols & Foster 2007). Case C2 has a moderate Reynolds number of $Re = 2500$. Nevertheless, this Reynolds number is above the Reynolds number range considered in the DNS study of Blondeaux *et al.* (2004) (cf. table 1) where the flows were still turbulent. Therefore, the selected configurations allow us to investigate the Reynolds number effects in turbulent oscillatory flows over moderate-sized vortex ripples.

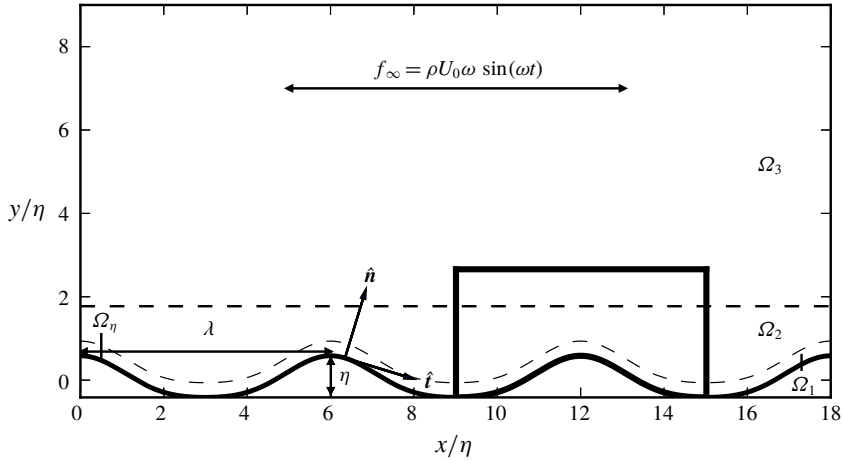


FIGURE 1. Two-dimensional side view of the flow domain. The thick solid lines indicate the region shown in figure 2. The dashed lines separate subdomains Ω_1 , Ω_2 , Ω_3 where different mesh configurations or element-polynomial orders are employed, cf. figure 2 and table 3. Terms \hat{i} and \hat{n} are the unit vectors that are in the tangential and normal directions on the ripple surface, respectively (scale for implication only).

2.2. Computational details

The two-dimensional side view of the computational domain is shown in figure 1. It contains three ripples, i.e. has a streamwise dimension of $x \in [0, L_x = 3\lambda = 18\eta]$. It has a significant spanwise dimension of $z \in [0, L_z = 6\lambda = 36\eta]$ and has the top boundary at $y = L_y = 1.5\lambda = 9\eta$. Periodicity is applied in streamwise and spanwise directions. Ripple surfaces are hydrodynamically smooth, i.e. $\mathbf{u} = 0$ for $\mathbf{x} \in \Omega_\eta$, and a symmetry boundary condition is applied on the top boundary. The governing equations (2.1) and (2.2) supplemented with these boundary conditions are discretized and solved using the Nektar++ code, a high-order spectral/hp element library developed by Cantwell *et al.* (2015). To this end, we employ a mixed representation, where a bi-dimensional spectral-element discretization is used in streamwise–wall-normal (x – y) plane, and global Fourier expansions are considered in the spanwise (z) direction, cf. Karniadakis (1990).

The element sizes along with other computational details are summarized in table 3. A mesh with 15 685 quadrilateral elements is employed for the spectral-element discretization, cf. figure 2. The mesh contains a structured region (Ω_1) of 300×15 elements near the bottom wall, and an unstructured region ($\Omega_2 \cup \Omega_3$) above. The streamwise grid spacing in the structured mesh (Ω_1) is calculated in local ripple coordinates, as the mesh follows the curvature of the ripple surface. To this end, Δx is the streamwise-tangent grid spacing in Ω_1 . Δy is the vertical grid spacing in Ω_1 . The grid is clustered towards the wall in Ω_1 with an expansion ratio of 1.175 between adjacent elements in the vertical direction. It is quite anisotropic near the wall with a factor of $\Delta x/\Delta y \approx 10$ and becomes isotropic close to the border to Ω_2 . In the unstructured mesh region ($\Omega_2 \cup \Omega_3$), we use a representative grid spacing

$$\Delta l = \frac{\mathcal{A}_e^{1/2}}{N_p}, \tag{2.6}$$

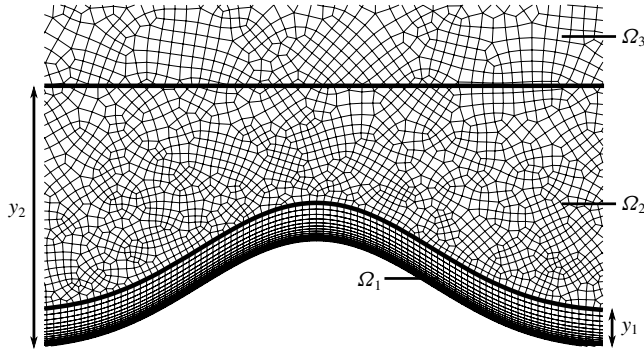


FIGURE 2. Overview of the elemental decomposition with quadrilateral elements. The structured mesh region Ω_1 is located between $[y_\eta, y_\eta + y_1]$, where $y_1 = 0.35\eta$. The regions above, i.e. Ω_2 and Ω_3 , contain an unstructured mesh. These two regions, separated by a line at $y_2 = 2.19\eta$, have different element-polynomial orders in Case C1, cf. table 3.

Cases	C1	C2
L_x, L_y, L_z	$3\lambda(18\eta), 1.5\lambda(9\eta), 6\lambda(36\eta)$	$3\lambda(18\eta), 1.5\lambda(9\eta), 6\lambda(36\eta)$
$N_{el}(\Omega_1) = N_x \times N_y, N_{xy}(\Omega_2 \cup \Omega_3)$	$300 \times 15, 11\ 185$	$300 \times 15, 11\ 185$
$N_p(\Omega_1), N_p(\Omega_2), N_p(\Omega_3)$	6, 7, 5	4, 4, 4
N_z	2160	1080
Total number of grid points	1.23×10^9	2.71×10^8
$\Delta x/\delta_s$	$0.142 \leq \Delta x/\delta_s \leq 0.166$	$0.106 \leq \Delta x/\delta_s \leq 0.124$
$\Delta y/\delta_s$	$0.014 \leq \Delta y/\delta_s \leq 0.135$	$0.011 \leq \Delta y/\delta_s \leq 0.101$
$\Delta l/\delta_s$	$0.043 \leq \Delta l/\delta_s \leq 0.869$	$0.032 \leq \Delta l/\delta_s \leq 0.543$
$\Delta z/\delta_s$	0.236	0.236
$\Delta t/T$	1/128 000	1/48 000
$T^i/T, T^s/T$	6, 5	6, 10

TABLE 3. Numerical parameters for the DNS studies. N_{el} is the number of spectral elements, N_p is the polynomial order for the modified Legendre basis and N_z is the number of Fourier modes in the spanwise direction. The total number of grid points is calculated with $N_{el} \times N_p^2 \times N_z$. The mesh consists of three regions, cf. figure 2, Δx and Δy are the spacings in the structured mesh located in Ω_1 , and Δl is the spacing in the unstructured mesh in $\Omega_2 \cup \Omega_3$, cf. (2.6). The term $\delta_s = \sqrt{2\nu/\omega}$ is the Stokes length. T is the flow period. T^i and T^s are the time intervals for initialization and sampling, respectively.

where \mathcal{A}_e is the area of the spectral element, and N_p is the polynomial order of the element. In the spanwise direction, equidistant collocation points are used for Fourier expansions with $N_z = 2160$ and $N_z = 1080$ for Cases C1 and C2, respectively.

To utilize the mixed Fourier spectral/hp element representation in the solution of Navier–Stokes equations, we first apply the Fourier expansion

$$\mathbf{u}(x, y, z, t) = \sum_{\kappa_z} \hat{\mathbf{u}}(x, y, \kappa_z, t) e^{i\kappa_z z}, \tag{2.7}$$

where κ_z is the wavenumber in the spanwise direction. This expansion is introduced into the governing equations. The 2/3 rule is applied to avoid aliasing errors (Boyd

2001). Subsequently, the resulting equations are further discretized in the x - y plane using a continuous-Galerkin projection where local element expansions are employed using the modified Legendre basis (Szabó, Düster & Rank 2004; Karniadakis & Sherwin 2005). In Case C1, the polynomial orders of the elements in different mesh regions are $N_p = 6$ in Ω_1 , $N_p = 7$ in Ω_2 and $N_p = 5$ in Ω_3 . The slightly higher expansion order in Ω_2 was found necessary for fully resolving the flow features and prevent instabilities due to underresolution. In Case C2, the polynomial order $N_p = 4$ is applied everywhere in the domain.

The resulting system of differential algebraic equations is discretized in time using a second-order scheme, in which both advection and diffusion terms are treated implicitly, cf. Vos *et al.* (2011) for details. A fixed time-step size Δt is chosen for both cases, where $\Delta t/T = 1/128\,000$ for C1 and $\Delta t/T = 1/48\,000$ for C2. The maximum Courant–Friedrichs–Lewy (CFL) number in both cases remained below 0.45. Finally, the coupled linear system of equations is segregated using a velocity correction scheme (Karniadakis, Israeli & Orszag 1991), and individual parts are solved using an iterative solver based on static condensation with a tolerance of 10^{-9} .

In order to trigger the transition to turbulence, the cases are initialized with random low-amplitude perturbations ($\|\mathbf{u}'\| \leq 0.0001U_0$) seeded on the y - z plane, which are uniform in the streamwise direction. Transition to turbulence has been observed around $t = T/4$. The flow is observed to reach a periodic state in 6 periods, i.e. $T^i = 6T$. Afterwards, we collected 64 three-dimensional snapshots per cycle for statistical analysis. This second phase lasted five periods in Case C1 ($T^s = 5T$) and 10 periods in C2 ($T^s = 10T$). Consequently, a database containing around 26 terabytes of flow data was produced.

The simulations are run on ASPIRE 1, the petascale supercomputer of the National Supercomputer Center of Singapore (NSCC). We have used Intel Xeon dual socket E5-2690v3 CPUs, where 2160 cores were employed for Case C1, and 960 cores for Case C2. Parallelization was achieved with message passing interface (MPI). Cases C1 and C2 required approximately 13 and 5 terabytes of memory during runtime. With this configuration, a time step lasted around 9 s and 3.5 s for Cases C1 and C2, respectively. The overall runtime cost of the simulations was over 10×10^6 CPU hours.

2.3. Grid assessment

In order to validate our DNS experiments, we will investigate the representation of the smallest and largest scales of the flow in the chosen grids and computational domain. The spatial resolution will be assessed in this section. A more detailed investigation using energy spectra is presented in appendix A. The domain size is accessed in appendix B. Finally, some comparisons to experimental measurements are made in appendix C.

We start with the analysis of near-wall resolutions. The essential quantities in the inner wall layer are the wall units, i.e. the kinematic viscosity ν , and the local friction velocity $u_\tau = \sqrt{\langle \tau_i \rangle / \rho}$, which is calculated using the streamwise component of the phase-averaged shear stress $\langle \tau_i \rangle$ on the wall. A local viscous length scale $\delta_\nu = \nu / u_\tau$ is defined using these wall units. Consequently, any length can be expressed in wall units using δ_ν , i.e. $l^+ = l / \delta_\nu$, where the superscript ‘+’ indicates scaling in wall units. The near-wall resolutions can be justified by analysing the grid spacings in wall units. To this end, the tangential grid spacing to the ripple surface (Δx) and the constant spanwise grid spacing (Δz) are employed to test the resolution in the streamwise and

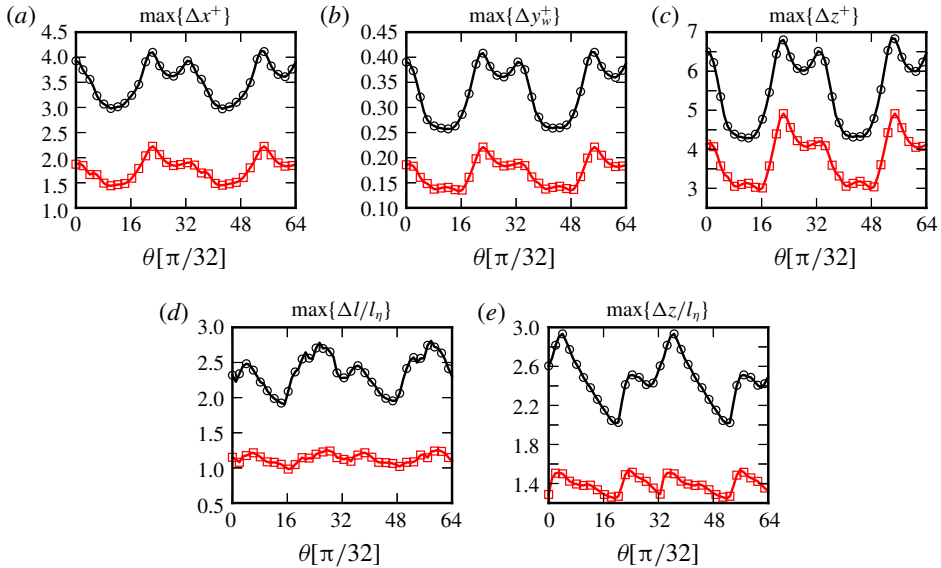


FIGURE 3. (Colour online) Extremal grid spacings over a flow cycle. (a–c) Largest grid spacings on the wall in wall units. Δy_w is the vertical distance of the first grid point from the ripple surface. (d,e) Largest grid spacings in free stream in Kolmogorov units ($l_\eta = (\nu^3/\varepsilon)^{1/4}$). Δl is the representative grid spacing in the unstructured hp-FEM mesh, cf. (2.6). (–○): Case C1; (–□): Case C2.

spanwise directions, respectively. In the highly non-uniform vertical direction, the first quadrature points from the ripple surface (Δy_w) are selected. Figure 3(a–c) shows the coarsest wall-layer resolutions over the cycle in wall units. In spectral-element discretizations, Karniadakis & Sherwin (2005) suggest to resolve the first nine wall units away from the wall with at least ten collocation points. Figure 3(b) shows that this criterion is well satisfied for both cases, as $\Delta y_w^+ \leq 0.41$ for Case C1 and $\Delta y_w^+ \leq 0.22$ for Case C2. Standard values for the streamwise and spanwise grid resolutions in recent DNS studies of wall-bounded flows are in the range $\Delta x^+ \approx 12$ and $\Delta z^+ \approx 6$, e.g. Hoyas & Jiménez (2006) employed (12.3, 0.323, 6.1) and Lozano-Durán & Jiménez (2014) employed (12.8, 0.314, 6.4) for $(\Delta x^+, \Delta y_w^+, \Delta z^+)$ resolutions, respectively. Figure 3(a,c) shows that the resolutions in these directions are well within these ranges for both cases. Moreover, our streamwise resolution is finer with $\Delta x^+ \leq 4.1$ for Case C1 and $\Delta x^+ \leq 2.2$ for Case C2, as we have to resolve the additional effects due to streamwise pressure gradients and the curvature of the ripple.

In free stream, the smallest eddies in the dissipation range have to be resolved. According to Kolmogorov's first hypothesis of similarity (Kolmogorov 1941), the local isotropic Kolmogorov microscale $l_\eta = (\nu^3/\varepsilon)^{1/4}$ is the length scale of the smallest eddies where ε is the local dissipation rate, cf. (4.4). The spectral elements are unstructured and approximately isotropic in regions Ω_2 and Ω_3 where coherent vortices spend most of their lives. Therefore, the resolution in the x - y plane is checked by comparing the local l_η to the element length scale Δl (cf. (2.6)). In the spanwise direction, a constant spacing Δz is used. The largest free-stream resolutions over the cycle are plotted in figure 3(d,e). We see that grid spacings are of the order

of the Kolmogorov scales with $\Delta l/l_\eta \leq 2.8$, $\Delta z/l_\eta \leq 2.9$ for Case C1, $\Delta l/l_\eta \leq 1.26$, and $\Delta z/l_\eta \leq 1.54$. Mahesh & Moin (1998) remarks that the smallest resolved length scale in a DNS is required to be $O(l_\eta)$, not l_η , as accurate first- and second-order statistics can be obtained when most of the dissipation is captured. In this regard, the selected spatial resolutions are sufficient for both cases, and we will show in appendix A that dissipation is also well captured.

3. Phase-locked vortex kinematics

In this section, we discuss the kinematics of wave-induced flow over ripples with a special emphasis on the motion of coherent spanwise vortices. In the considered oscillatory flow, ensemble averaging is approximated using phase-locked averaging combined with spatial averaging over homogeneous direction and ripple-based averaging, e.g. for velocity,

$$\langle \mathbf{u} \rangle(x, y, t) = \frac{1}{NM} \sum_{m=0}^{M-1} \sum_{n=0}^{N-1} \tilde{\mathbf{u}}(x + m\lambda, y, t + nT), \quad 0 \leq x < \lambda, 0 \leq t < T, \quad (3.1)$$

where $\tilde{\mathbf{u}}$ is the spatially averaged velocity over the homogeneous direction z , N is the total number of sampling periods and M is the number of ripples in the domain. Using this averaging, Reynolds decomposition is applied to the fields of interest, e.g. $\mathbf{u} = \langle \mathbf{u} \rangle + \mathbf{u}'$, where \mathbf{u}' is the fluctuating part of the turbulent velocity field.

Figures 4 and 5 show the phase-averaged spanwise vorticity $\langle \omega_z \rangle$ contours, i.e.

$$\langle \omega_z \rangle = \frac{\partial \langle u_y \rangle}{\partial x} - \frac{\partial \langle u_x \rangle}{\partial y}, \quad (3.2)$$

and velocity $\langle \mathbf{u} \rangle$ vectors along the half-cycle ($0 \leq \theta < \pi$) for cases C1 and C2, respectively. We will use the $\langle \omega_z \rangle$ -field to discuss the coherent-vortex kinematics. To this end, we define a coherent vortex as an enclosed region of concentrated $\langle \omega_z \rangle$. Similar definitions have previously been employed in the studies of turbulent coherent structures in free-shear flows, cf. e.g. Hussain (1986). The strength of a coherent vortex can be measured by its circulation, which is calculated by (Batchelor 2000)

$$\Gamma = \oint_C \langle \mathbf{u} \rangle \cdot d\mathbf{l} = \int_A \langle \omega_z \rangle dA, \quad (3.3)$$

where C is the closed curve representing the vortex boundary, and A is the area of the vortex region. We have selected the contours $|\langle \omega_z \rangle| = 0.15U_0/\eta$ as the boundary threshold for vortices. This value corresponds to the lowest contour level in figures 4 and 5, and it is approximately 2.5% of the maximum vorticity level in the figures. The circulation of coherent vortices is presented in parentheses in figures 4 and 5. These values can be compared with the total circulation around a single ripple, which can be calculated using a line integral on a closed curve containing the ripple surface, vertical lines normal to the troughs and a horizontal line in the free stream. In our cases, the total circulation at a phase equals to $\Gamma_R = -u_0\lambda = -6u_0\eta$.

Figure 6(a,b) further shows the vorticity distributions on the ripple surface Ω_η , i.e.

$$\langle \omega_z(\mathbf{x}, \theta) \rangle = -\frac{\partial \langle \mathbf{u}(\mathbf{x}, \theta) \rangle}{\partial \mathbf{x}} \cdot \hat{\mathbf{n}} \quad \text{for } \mathbf{x} \in \Omega_\eta, \quad (3.4)$$

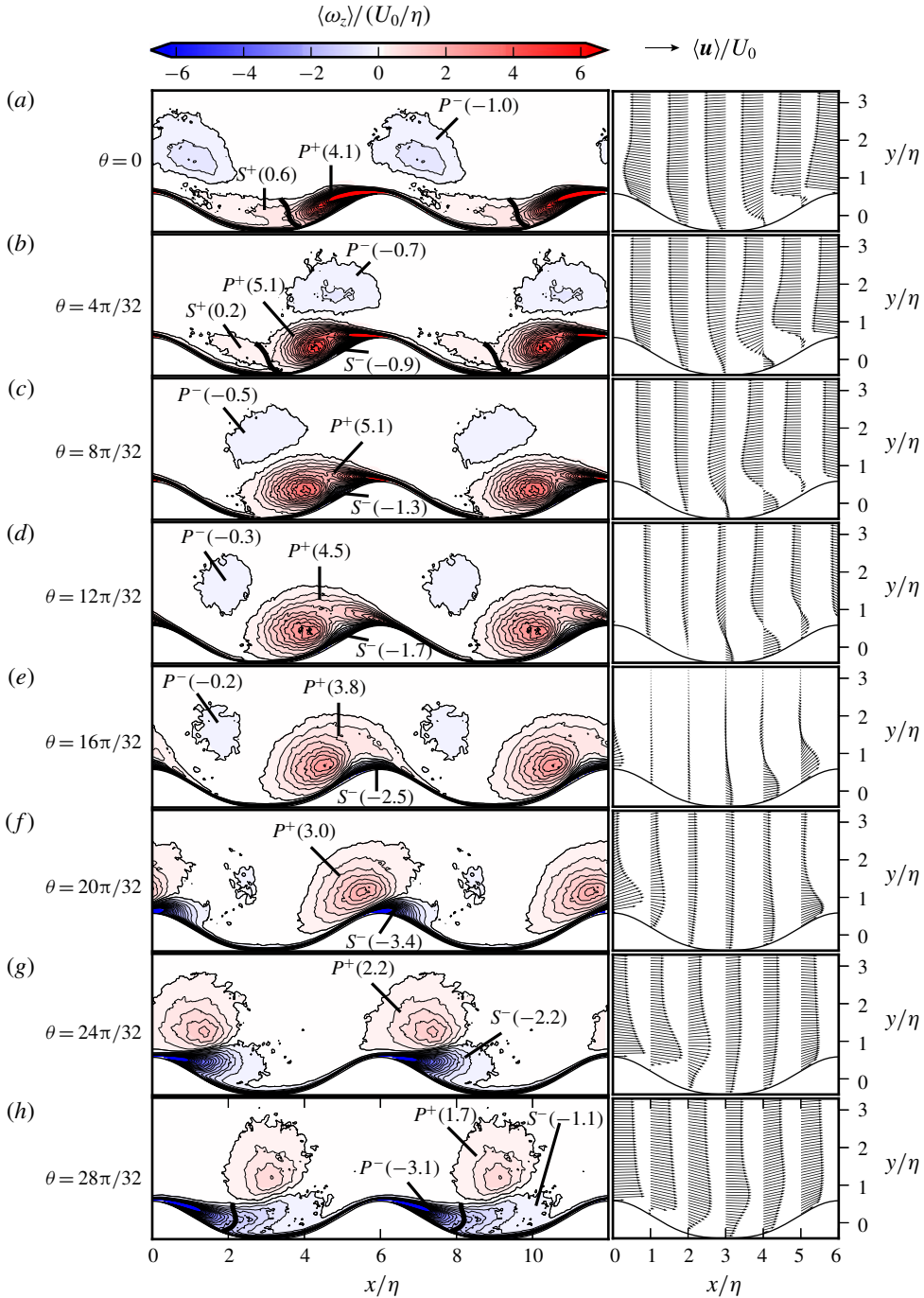


FIGURE 4. (Colour online) (a–h) Evolution of vorticity and velocity fields along the half-cycle for Case C1. (Left) Contours of phase-averaged spanwise vorticity $\langle \omega_z \rangle$; (right) the phase-averaged velocity $\langle \mathbf{u} \rangle$ vectors. The values in parentheses show the normalized circulation $\Gamma/U_0\eta$ of the vortices, cf. (3.3). The thick lines show a section of the isolines $\langle p \rangle$, which are employed to separate P^- and S^- vortices; (a,b) $\langle p \rangle / \rho U_0^2 = 0.2$ and (h) $\langle p \rangle / \rho U_0^2 = 0.075$.

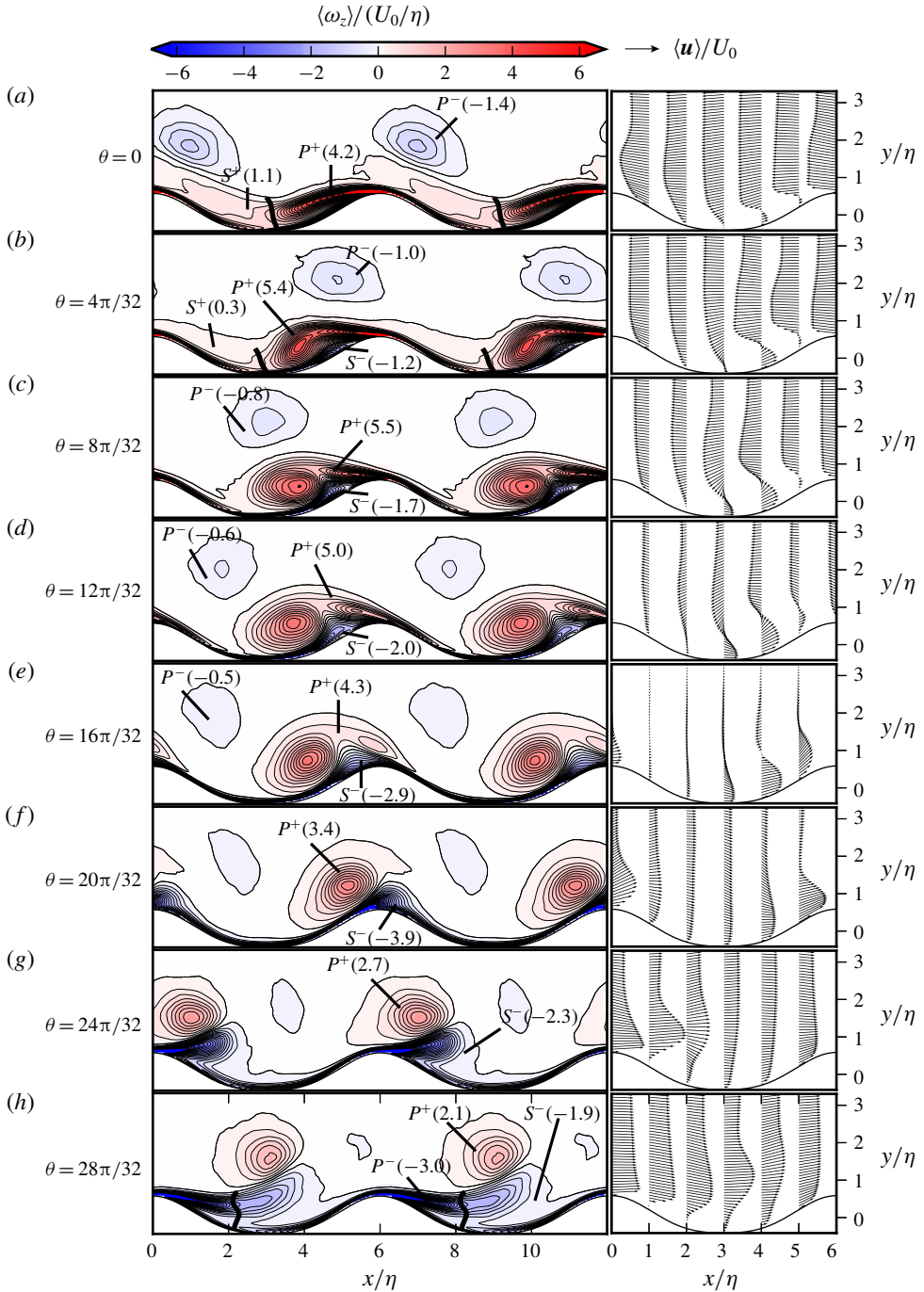


FIGURE 5. (Colour online) Evolution of vorticity and velocity fields along the half-cycle for Case C2. See figure 4 for captions.

where \hat{n} is the normal of the ripple surface (cf. figure 1 for its orientation). In these figures, we consider $\langle \omega_z \rangle = 0$ (thick solid lines) as the average position of the separation and reattachment points.

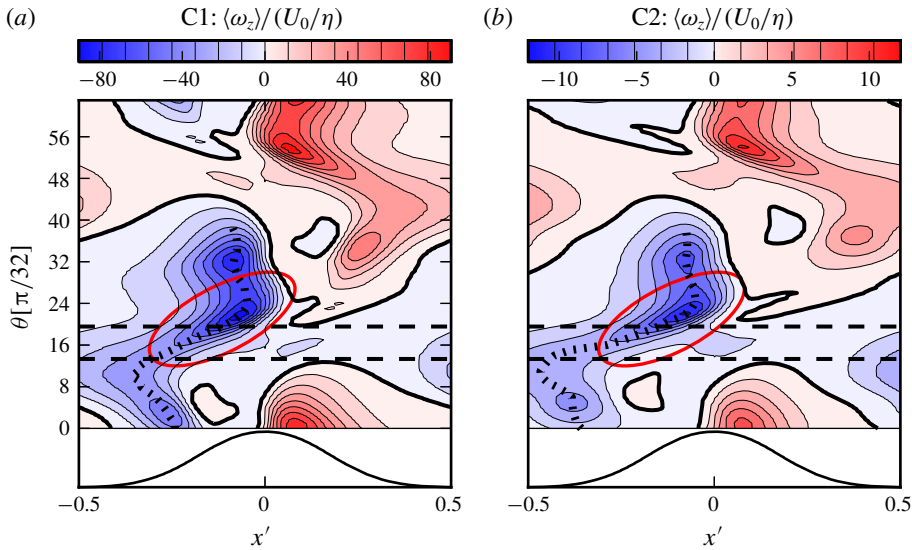


FIGURE 6. (Colour online) Distribution of the phase-averaged spanwise vorticity $\langle \omega_z \rangle$ on the ripple surface around the cycle. The thick solid lines show $\langle \omega_z \rangle = 0$. The dashed lines bound the time interval without flow separation. The dotted lines show the position of the minimum vorticity on the ripple for $0 \leq \theta \leq 40\pi/32$. A local ripple coordinate $x' = (x - x_c)/\lambda$ is employed with x_c being the streamwise location of the ripple crest.

We will discuss the deceleration and acceleration phases in §§3.1 and 3.2, respectively. In the deceleration phase between $0 \leq \theta < \pi/2$ (figures 4a–d and 5a–d). In this stage, new vortices form and start absorbing the flow energy. Therefore, we will also denote the deceleration phase as the vortex-formation phase. In the acceleration stage in the interval $\pi/2 \leq \theta < \pi$ (figures 4e–h and 5e–h), the coherent vortices travel large distances with their self-induced velocities, and produce jet-like flows. We will denote the acceleration phase as the jet ejection, or simply ejection, phase.

3.1. Vortex-formation (deceleration) phase ($0 \leq \theta < \pi/2$)

At the start of deceleration phase at $\theta = 0$, where the free-stream velocity is at its negative peak (cf. figures 4a and 5a), the flow separates at the crest of the ripple ($x' = 0$) and reattaches at $x' \approx -0.4$ ($x' = (x - x_c)/\lambda$ where x_c is the streamwise location of the crest) for Case C1, cf. figure 6(a). The reattachment point in Case C2 is further downstream at the stoss side at around $x' \approx 0.4$, cf. figure 6(b). The positive-vorticity flux from the crest feeds the forming vortex in the lee of the ripple. We denote this vortex P^+ , where P stands for primary vortex, and the superscript ‘+’ indicates the positive circulation – not to be confused with the wall units superscript. Furthermore, there is a secondary vortex from previous half-cycle (S^+) with the same sense of circulation. In order to distinguish these vortices, we employ a segment of the pressure isoline $\langle p \rangle / \rho U_0^2 = 0.2$, cf. the thick solid lines in figures 4(a,b) and 5(a,b). This practical selection is based on the observation that the ejected secondary vortex quickly loses its property of being a low-pressure centre after being detached from the ripple crest. Moreover, the boundary layer beneath the S^+ -vortex contains the same sign of vorticity with the vortex. In order to differentiate the boundary layer

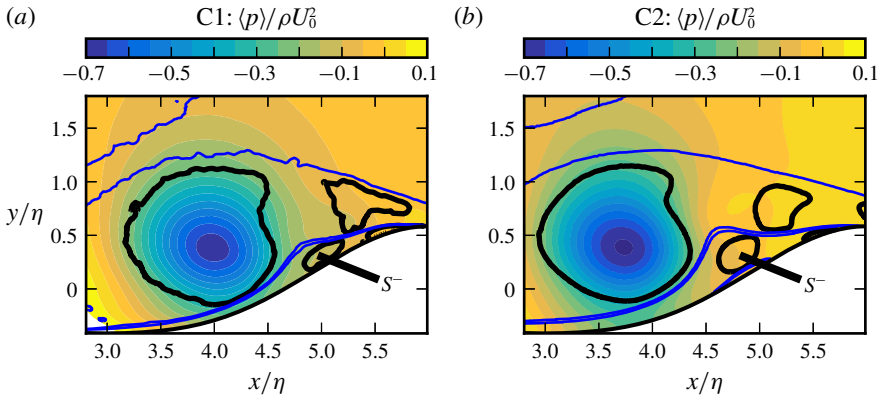


FIGURE 7. (Colour online) Formation of the secondary spanwise vortex S^- via flow separation induced by the adverse pressure gradient in the primary vortex P^+ at $\theta = 8\pi/32$. Shaded contours show $\langle p \rangle / \rho U_0^2$. The thick contour lines are $\Lambda = 1/2(\Omega_{ij}\Omega_{ij} - S_{ij}S_{ij}) = 0$. Blue contours show $\langle \omega_z \rangle / (U_0/\eta) = |\pm 0.15|$ indicating the coherent-vortex boundaries.

and vortex regions, we exclude the wall layer of $\Delta y = 2\delta_s$ thickness from the circulation field of the S^+ -vortex. At $\theta = 0$, there is another primary vortex, P^- , moving to the west above the ripple crest. It has formed in the previous half-cycle on the eastern side of the eastern neighbour, hence has a negative circulation. This residual vortex has around 25% and 33% circulation of P^+ -vortices in Cases C1 and C2, respectively. This suggests a small but non-negligible flow interference between neighbouring ripples.

We further see at $\theta = 0$ that P^+ -vortex induces a thin boundary layer on the wall with reverse circulation, cf. the negative vorticity contours at the lee side ($x' < 0$) in figure 6(a,b). While the vorticity flux at the crest keeps increasing the circulation of P^+ , the reverse flow becomes also stronger, cf. S^- in figures 4(b,c) and 5(b,c). Furthermore, the low-pressure zone in the P^+ -vortex intensifies, and a strong adverse pressure gradient is created along the ripple surface at the lee side. This is shown in figure 7 for both cases at phase $\theta = 8\pi/32$. The adverse pressure gradient along the wall yields a secondary flow separation within the vortex-induced boundary layer, cf. positive-vorticity islands at the lee side ($x' < 0$) in $2\pi/32 \leq \theta \leq 9\pi/32$ for C1 and in $4\pi/32 \leq \theta \leq 12\pi/32$ for C2 in figure 6(a,b). Following the separation, S^- rolls into a secondary separation bubble. Figure 7 demonstrates this using the Okubo–Weiss parameter $\Lambda = 1/2(\Omega_{ij}\Omega_{ij} - S_{ij}S_{ij})$, where $\Omega_{ij} = 1/2(\partial \langle u_i \rangle / \partial x_j - \partial \langle u_j \rangle / \partial x_i)$ is the phase-averaged rate of rotation tensor, $\Omega_{ij}\Omega_{ij} = 1/2\langle \omega_z \rangle^2$ in two dimensions and

$$S_{ij} = \frac{1}{2} \left(\frac{\partial \langle u_i \rangle}{\partial x_j} + \frac{\partial \langle u_j \rangle}{\partial x_i} \right) \tag{3.5}$$

is the phase-averaged rate of strain tensor. Positive values of Λ identify vortex cores where the vorticity prevails over strain (Okubo 1970; Weiss 1991). To this end, the isoline of $\Lambda = 0$ shows the development of secondary separation bubble in S^- for both cases in figure 7. General properties of secondary vortex development due to vortex-induced separation are discussed in Doligalski, Smith & Walker (1994). In the case of vortex ripples, the phenomenon has been documented previously by Blondeaux & Vittori (1991) in a two-dimensional setting. The coherent secondary vortex is not

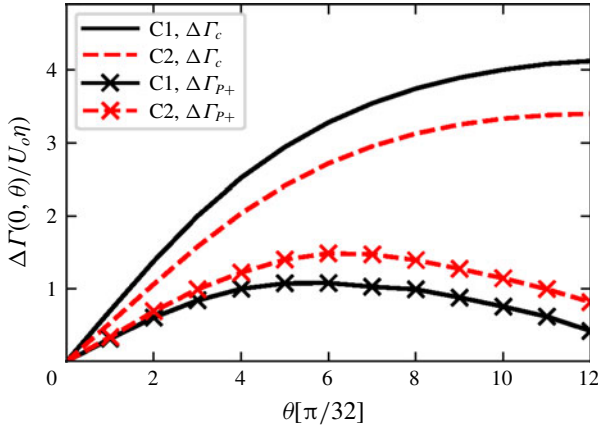


FIGURE 8. (Colour online) Comparison between the net shed circulation at the crest ($\Delta\Gamma_c(0, \theta)$, cf. (3.7)) and the absorbed circulation ($\Delta\Gamma_{P^+} = \Gamma_{P^+}(\theta) - \Gamma_{P^+}(0)$) in the primary vortex P^+ during its formation. Circulations are normalized by $U_0\eta$.

captured in studies with discrete vortex models, e.g. cf. Longuet-Higgins (1981), and sometimes not captured in experiments either, cf. e.g. Earnshaw & Greated (1998) and Fredsøe *et al.* (1999).

The coherent spanwise vortices are highly turbulent structures. Therefore, the amount of spanwise vorticity shed from the crest is considerably higher than that absorbed in the P^+ -vortex. This can be shown by comparing the shed and absorbed circulations in the temporal range with prominent flow separation, i.e. $0 \leq \theta < 12\pi/32$. To this end, the total positive-vorticity flux across the boundary layer above the crest, which is located at $(x_c, y_c = y_\eta(x_c))$, can be calculated using

$$\dot{\Gamma}_c = \int_{y_\eta(x_c)}^{y_\delta} \langle u_x(x_c, y) \rangle \langle \omega_z(x_c, y) \rangle dy, \tag{3.6}$$

where y_δ is the vertical coordinate of the peak streamwise velocity. Consequently, the total shed positive vorticity from the crest in a range $\theta_i \leq \theta \leq \theta_f$ is given by

$$\Delta\Gamma_c(\theta_i, \theta_f) = \int_{t=\theta_i/\omega}^{t=\theta_f/\omega} \dot{\Gamma}_c dt. \tag{3.7}$$

Figure 8 compares the net shed positive vorticity $\Delta\Gamma_c(0, \theta)$ with the net absorbed circulation in P^+ , i.e. $\Delta\Gamma_{P^+} = \Gamma_{P^+}(\theta) - \Gamma_{P^+}(0)$. We see that P^+ cannot keep most of the shed circulation, and the gap $\Delta\Gamma_c - \Delta\Gamma_{P^+}$ grows with time. In particular, $\Delta\Gamma_{P^+}$ starts to decay for both cases after $\theta > 6\pi/32$ showing that the loss of circulation due to turbulent diffusion dominates over the gain due to positive-vorticity flux from the crest. The shed circulation is higher in Case C1 but the overall absorbed vorticity in the primary vortex is less for this case. This suggests a more active turbulent dynamics in P^+ for C1. The turbulence properties of vortices will be discussed in § 5.

We see in figures 4(c,d) and 5(c,d) that the P^+ vortex grows and spreads vertically when the free-stream velocity further decelerates. Moreover, the passing residual vortex P^- pushes P^+ slightly away from the crest, and moves the reattachment point of P^+ further towards west to the stoss region, cf. $\langle \omega_z \rangle = 0$ contours in figure 6.

The motion of P^+ during its formation can also be tracked by the location of the most-intense vorticity on the ripple surface, cf. the dotted lines in figure 6. In this regard, P^+ moves towards the trough of the ripple until $\theta = 12\pi/32$, and then heads back to the crest, when its self-induction dominates over the weakening free-stream velocity. The boundary layer at the stoss side stops separating at $\theta = 14\pi/32$, and a reverse flow to the east follows subsequently on the whole ripple until around $\theta = 20\pi/32$. This regime without flow separation is indicated with dashed lines in figure 6.

3.2. Jet-ejection (acceleration) phase ($\pi/2 \leq \theta < \pi$)

When the free-stream velocity vanishes at $\theta = 16\pi/32$, the $P^+ - S^-$ vortex dipole is about to eject itself from the crest, cf. figures 4(e) and 5(e). The total circulation vanishes for this phase, i.e. $\Gamma_R = 0$, as the free-stream velocity u_0 vanishes. Therefore, the circulation contained in the near-wall layer is $\Gamma_v = -\Gamma_{P^+} - \Gamma_{P^-} - \Gamma_{S^-} = -1.1U_0\eta$ for Case C1, and $\Gamma_v = -0.9U_0\eta$ for C2. These negative values indicate the phase difference between the free stream and the wall shear.

We have discussed in §3.1 that P^+ changes its convection direction ahead of the free-stream flow reversal at $\theta = 14\pi/32$, and moves towards the crest with its self-induced velocity. P^+ is stretched along an axis roughly parallel to the ripple slope during this process, and deforms into an elliptic geometry. The velocity fields in figures 4(e) and 5(e) further show that the self-induced motion produces a wall jet. This wall jet induces high shear on the wall at the footprint of the vortex, cf. encircled regions with red lines in figure 6. Further in the cycle $\theta = 20\pi/32$, the $P^+ - S^-$ vortex dipole ejects itself over the ripple, cf. $\langle \mathbf{u} \rangle$ vectors in figures 4(f) and 5(f). The resulting jet is very strong with a peak velocity magnitude of approximately $2U_0$. Due to this strong jet, the maximum values in the local wall vorticity, and analogously in the local wall shear stress (cf. §5.3 for details), are observed during the ejection process. The free jet resulting from the ejection is inclined with an angle approximately parallel to the ripple slope. While detaching from the crest, the jet and the trajectory of the vortex pair become less inclined, cf. figures 4(g) and 5(g). We note that the ejection angle is steeper in Case C2. The size and the orientation of the S^- vortex appear to lead to this Reynolds number effect. The S^- vortex occupies significantly more space in C2 compared to the one in C1 due to larger boundary-layer thickness, and is more detached from the wall, cf. figure 7(a,b). Consequently, the induced velocities by the $P^+ - S^-$ pair are more inclined in C2, leading to a steeper ejection angle. The ejection angle has important consequences on the turbulent dynamics, which will be discussed in §5.

When the vortex pair completely detaches from the crest, a new primary vortex forms at its trail, cf. P^- vortices in figures 4(h) and 5(h). The detached vortices travel to the east in an approximately horizontal trajectory. In this process, S^- loses its circulation at a higher rate than P^+ due to interactions with the wall. This effect is less pronounced in C2, i.e. $\Gamma_{S^-} = -1.9$ in C2, whereas $\Gamma_{S^-} = -1.1$ in C1. This is due to steeper ejection angle leading a higher altitude vortex trajectory in C2, which limits the wall interference.

4. Space- and time-averaged turbulence statistics

To give a global picture, we will analyse now spatially or temporally averaged fields. The main emphasis will be on the budget terms of turbulent kinetic energy (TKE)

$k = \langle u'_i u'_i \rangle / 2$. The transport equation for TKE reads as follows:

$$\frac{\partial k}{\partial t} + \frac{\partial(\langle u_i \rangle k + \mathcal{T}_i)}{\partial x_i} = \mathcal{P} - \varepsilon, \tag{4.1}$$

where

$$\mathcal{T}_i = \frac{1}{2} \langle u'_i u'_j u'_j \rangle + \langle u'_i p' \rangle / \rho - 2\nu \langle u'_j s'_{ij} \rangle \tag{4.2}$$

contains the turbulent transport terms,

$$\mathcal{P} = -\langle u'_i u'_j \rangle \frac{\partial \langle u_i \rangle}{\partial x_j} \tag{4.3}$$

is the turbulent-production term, and

$$\varepsilon = 2\nu \langle s'_{ij} s'_{ij} \rangle \tag{4.4}$$

is the turbulent dissipation term. In (4.2) and (4.4), s'_{ij} is the fluctuating rate of strain:

$$s'_{ij} = \frac{1}{2} \left(\frac{\partial u'_i}{\partial x_j} + \frac{\partial u'_j}{\partial x_i} \right). \tag{4.5}$$

We start with the analysis of global TKE-budget. The global TKE-budget for a ripple can be obtained by spatially integrating individual terms in a periodic two-dimensional domain occupying the computational region between a ripple and the top boundary, i.e. $\mathcal{V} := [0, \lambda] \times [y_\eta, L_y = 1.5\lambda]$. As a result of this integration, the divergence terms on the left-hand side of (4.1) vanish, i.e.

$$\int_{\mathcal{V}} \frac{\partial(\langle u_i \rangle k + \mathcal{T}_i)}{\partial x_i} dx dy = \int_S n_i (\langle u_i \rangle k + \mathcal{T}_i) dx dy = 0, \tag{4.6}$$

as velocity fluctuations vanish on the top boundary and the ripple wall, and the contributions on the periodic boundaries cancel out. Consequently, the local balance in (4.1) is transformed into the following simplified global form

$$\frac{dk_{\mathcal{V}}}{dt} = \mathcal{P}_{\mathcal{V}} - \varepsilon_{\mathcal{V}}, \tag{4.7}$$

where $k_{\mathcal{V}} = \int_{\mathcal{V}} k dx dy$, $\mathcal{P}_{\mathcal{V}} = \int_{\mathcal{V}} \mathcal{P} dx dy$ and $\varepsilon_{\mathcal{V}} = \int_{\mathcal{V}} \varepsilon dx dy$ are global turbulent kinetic energy, production and dissipation, respectively, and are scalar functions of time.

Figure 9 shows the intra-period variations of $\mathcal{P}_{\mathcal{V}}$ and $\varepsilon_{\mathcal{V}}$ for both cases. We see two production peaks in a half-cycle, one at approximately $\theta = 4\pi/32$ and another at $\theta = 24\pi/32$. The first peak (\mathcal{P}_{max}^1) is roughly at the beginning of the vortex-formation stage, when the free-stream velocity is strong, and the circulation of P^+ -vortex starts to saturate. The second peak (\mathcal{P}_{max}^2) is in the ejection phase, and corresponds to the phase when the primary vortex, along with the secondary vortex, is washed over from the ripple (cf. figures 4g and 5g).

There is a Reynolds number effect on the production peaks, especially for \mathcal{P}_{max}^1 . The value of \mathcal{P}_{max}^1 in Case C1 is approximately double that of Case C2. The difference in \mathcal{P}_{max}^2 remains approximately 20%. Moreover, the two production peaks in Case C2 are of similar magnitude, where \mathcal{P}_{max}^1 clearly dominates in Case C1. Furthermore, the

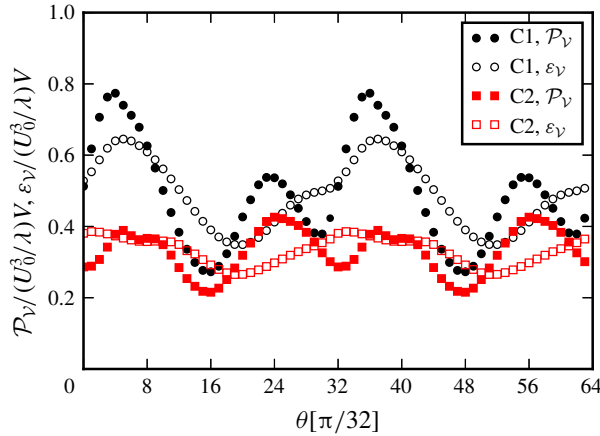


FIGURE 9. (Colour online) Evolution of global TKE production \mathcal{P}_V and dissipation ε_V along the cycle, cf. (4.7). For normalization we employed the area $V = \lambda\eta$.

vortex formation stage dominates the overall k -production in Case C1, where both vortex formation and ejection stages make similar contributions to k in Case C2.

We consider now time-averaged fields for a preliminary analysis of spatial distributions. Time averaging is defined as follows, e.g. for k ,

$$\bar{k}(x, y) = \frac{1}{T} \int_0^T k(x, y, t) dt. \tag{4.8}$$

Figure 10 shows the time-averaged TKE \bar{k} , production $\bar{\mathcal{P}}$ and dissipation $\bar{\varepsilon}$ for both cases. In addition to TKE-budget terms, we also consider the time-averaged fluctuating enstrophy $\bar{\mathcal{E}} = \overline{\omega'_i \omega'_i} / 2$. All fields are normalized with their respective peak value, hence the contours vary between $[0, 1]$.

Figure 10(a) shows that \bar{k} is concentrated in the regions where lee vortices form during the cycle. The turbulent kinetic energy in the near-wall region is considerably lower than that in the vortex regions. This suggests that the wall turbulence is less dominant in the overall dynamics for the selected flow configurations – a condition that might change in higher Reynolds numbers or in the presence of rough walls. In general, \bar{k} in C1 remains more localized around the ripple compared to the \bar{k} in C2. This is due to vortices reaching higher altitudes in the free stream in Case C2 thanks to the steeper ejection angle of the $P^+ - S^-$ vortex dipole.

Figures 10(b) and 10(d) show that $\bar{\mathcal{E}}$ and $\bar{\varepsilon}$ have very similar distributions in Case C1, as both vorticity and strain rate are small-scale quantities, which deliver similar average fields in high Reynolds number turbulence (Tennekes & Lumley 1972). These fields show more noticeable differences in C2 due to the relatively low Reynolds number. For these terms, the highest values are located in the vicinity of the wall, which is not resolved in figure 10(b,d). Therefore, the upper end of the colour scale is selected to be 0.3 to enhance the presentation of the distributions in the free stream in figure 10(b,d). The time-averaged production rate peaks at the crests, cf. figure 10(c). In the free-stream region, $\bar{\mathcal{P}}$ has a similar organization to the dissipation rate in Case C2, while in C1 it concentrates mainly in the separating layer, which is more horizontally distributed compared to the one in C2. Furthermore, the

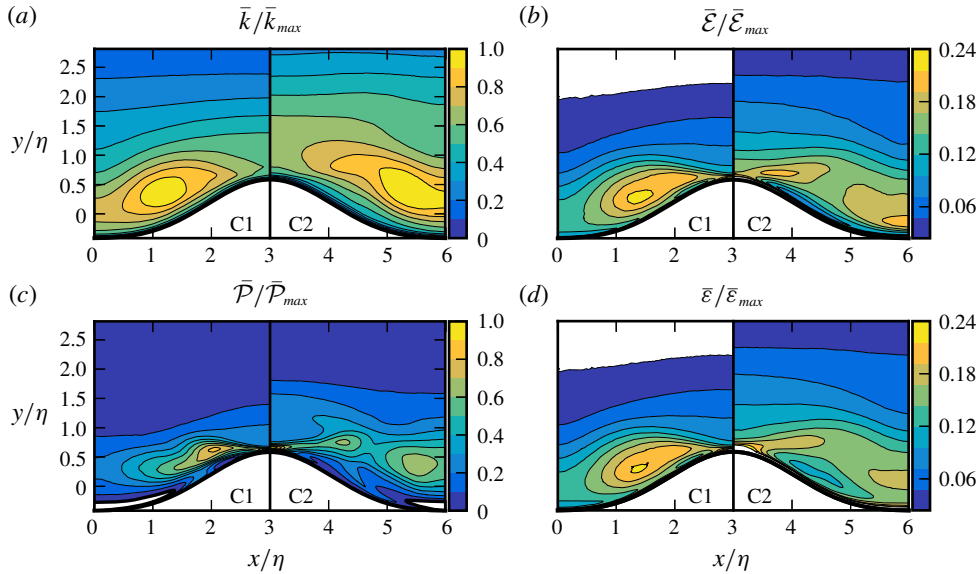


FIGURE 10. (Colour online) Time-averaged turbulent flow fields. The fields are symmetric with respect to the crest plane at $x/\eta = 3$. The thick isolines near troughs in (c) indicate $\bar{\mathcal{P}} = 0$. Below these lines the production rates are negative.

average production rate in the regions close to the troughs is negative in both cases meaning that the mean flow receives its energy from turbulence in these regions.

In summary, figure 10 shows that the turbulent kinetic energy in Case C1 is produced in separated shear layers, and is dissipated in the core of lee vortices. The spatial separation among production and dissipation regions is typical for coherent large-scale vortices in high Reynolds numbers, as shown by Hussain (1986) for turbulent mixing layers and jets. The lack of this physical separation in C2 is an effect of the low Reynolds number. Blondeaux *et al.* (2004) previously observed similar overlaps between production and dissipation zones in the case of oscillatory flow over vortex ripples at low Reynolds numbers.

5. Phase-locked turbulence statistics

In this section, we investigate how the TKE-budget terms (4.1)–(4.4) vary over a flow cycle. The focus is on the terms contributing to the global budget in (4.7), i.e. k , \mathcal{P} and ε . Furthermore, additional turbulence statistics at several representative locations will be analysed to gain further insights into the turbulence dynamics. To this end, we consider anisotropies using the invariants

$$\Pi_b = -\frac{1}{2}b_{ij}b_{ji}, \quad \Pi_v = -\frac{1}{2}v_{ij}v_{ji}, \tag{5.1a,b}$$

where b_{ij} and v_{ij} are the anisotropy tensors for velocity and vorticity, respectively, i.e.

$$b_{ij} = \frac{\langle u'_i u'_j \rangle}{\langle u'_i u'_i \rangle} - \frac{1}{3}\delta_{ij}, \quad v_{ij} = \frac{\langle \omega'_i \omega'_j \rangle}{\langle \omega'_i \omega'_i \rangle} - \frac{1}{3}\delta_{ij}. \tag{5.2a,b}$$

The absolute value of the invariants range between 0 (isotropic field) and 1/3 (perfect alignment to one direction) (Lumley 1979). Furthermore, we consider the parameter

$$K = \frac{2\langle u_x'^2 \rangle}{\langle u_y' u_y' \rangle + \langle u_z' u_z' \rangle}, \quad (5.3)$$

where local coordinates (x', y', z') aligned with the local ensemble-averaged velocity vector are employed. Lee, Kim & Moin (1990) suggested $K > 5$ as an indicator for the presence of quasi-streamwise streaks in the velocity fields of turbulent shear flows. These low-speed streaks and accompanying flow structures have been previously shown to yield non-random preferential concentrations for particles near the wall (Rouson & Eaton 2001), hence they play a key role in sediment-transport processes. Another useful quantity is the shear-rate parameter (Corrsin 1958)

$$S^* = \frac{Sk}{\varepsilon}, \quad (5.4)$$

where $S = (2S_{ij}S_{ij})^{1/2}$. This parameter gives the ratio of turnover time of energy-containing eddies to the mean-deformation time scale; $S^* \gg 1$ indicates the dominance of the mean shear on the nonlinear turbulence dynamics.

5.1. Evolution of turbulent fields

Figures 11 and 12 show the distribution of the turbulent kinetic energy k , its production rate \mathcal{P} and its dissipation rate ε at four representative phases for Cases C1 and C2, respectively. The thick contours show $|\langle \omega_z \rangle| = 0.15U_0/\eta$ indicating the coherent-vortex boundaries. Figures 11(a–c) and 12(a–c) show the budget terms at $\theta = 4\pi/32$, when the first global production peak occurs (cf. figure 9). In Case C1, the turbulence is already well developed in the primary vortex P^+ (cf. figures 4 and 5 for vortex nomenclature), where k reaches values up to $0.35U_0^2$. In the free stream above the ripple, we see the residual vortex from the previous half-cycle, i.e. P^- , with considerably lower turbulent kinetic energy at around $k \approx 0.03U_0^2$. In contrast, P^+ and P^- vortices have much closer turbulence levels in C2, as turbulence at the lee side is not well developed yet for this case, cf. figure 12(a).

Figures 11(b) and 12(b) further show that the turbulence production concentrates in the separated shear layers from the crest. A set of turbulent quantities evaluated at locations where the production peaks (indicated with X_1 in figures) is presented in table 4. We see that the peak in C1 has approximately four times the production rate of the C2-peak (cf. also the difference in the global production rate in figure 9). This is mainly due to more intense turbulence on the lee side for Case C1, as mean strain rates have similar values in both cases, i.e. $S/(U_0/\lambda) \approx 36.9$, $k/U_0^2 \approx 0.21$ at X_1 in C1, and $S/(U_0/\lambda) \approx 33.5$, $k/U_0^2 \approx 0.07$ at X_1 in C2. The quantity kS is used here as a surrogate for production rate $\mathcal{P} = -\langle u_i' u_j' \rangle S_{ij}$, which is bounded by $|\mathcal{P}| \leq kS$. In parallel to the production rate, the dissipation rate also remains considerably lower for C2 compared to C1 at $\theta = 4\pi/32$.

With the deceleration of free-stream velocity, the turbulence production rate in the free-separated layers weakens, cf. the phase $\theta = 12\pi/32$ in figures 11(e) and 12(e). Two other production regions in this phase are the primary vortex core away from the wall and the secondary separation zone near the wall due to formation of the vortex S^- . Later, when the vortices eject themselves from the crest, the production

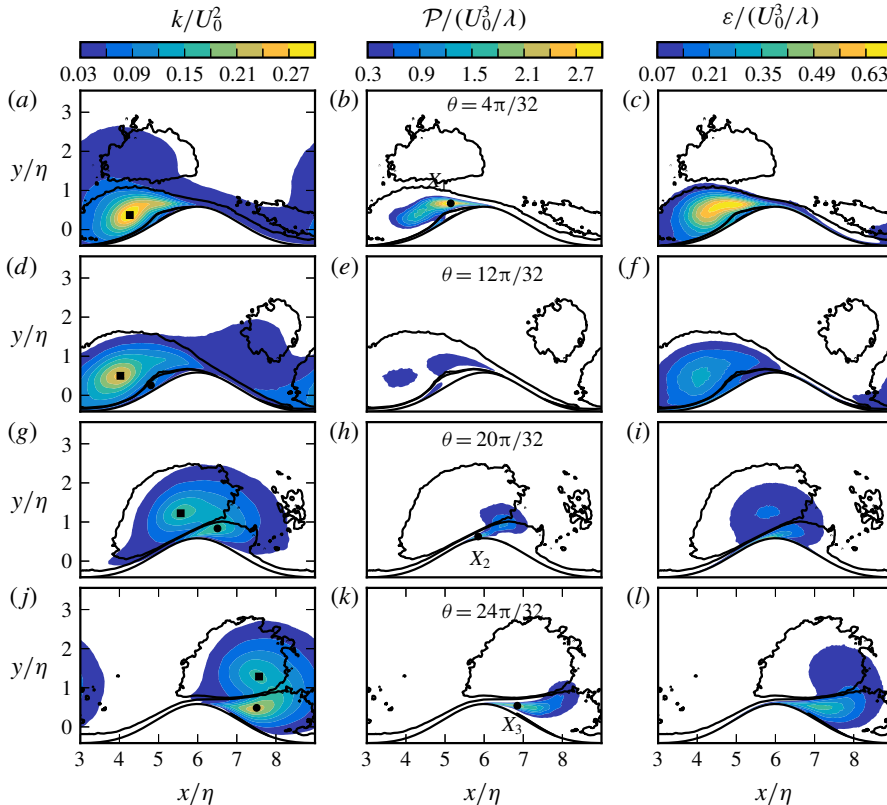


FIGURE 11. (Colour online) Evolution of selected TKE-budget terms in Case C1. Shaded contours indicate TKE ($k = \langle u_i' u_i' \rangle / 2$) (a,d,g,j), turbulent-production rate \mathcal{P} (b,e,h,k) and turbulent dissipation rate ε (c,f,i,l), and the thick isolines indicate $|\langle \omega_z \rangle| / (U_0 / \eta) = 0.15$. Markers in k -plots indicate the points where k peaks in coherent vortices; (O): S^- vortex; (\square): P^+ vortex. The trajectories of these points are shown in figure 15.

rate near the wall intensifies. The peak-production locations here are indicated as X_2 in figures 11(h) and 12(h). Table 4 shows that the production rate at X_2 is lower than X_1 in C1, while X_1 and X_2 have similar rates in C2.

We now turn to the turbulence properties at $\theta = 24\pi/32$ (figures 11j–l and 12j–l), where the second global production peak occurs in the half-cycle. This phase is characterized by the self-ejection of the $P^+ - S^-$ vortex dipole over the crest. Figures 11(j) and 12(j) show that k is mainly concentrated in the vortices. For the production and dissipation rate, C1 again leads over C2, but in this phase the differences are less pronounced compared to the first global production peak around $\theta = 4\pi/32$. The production rate peaks in the separated shear layer located in S^- vortex (indicated with X_3 in figures 11k and 12k).

The major difference between C1 and C2 at $\theta = 24\pi/32$ is the ejection angle of the vortex dipole $P^+ - S^-$, i.e. the angle is steeper in C2. This leads to essential differences in turbulent kinetic energy in further phases. This is shown using the evolution of k after the ejection of vortices, cf. figure 13(a–d) for Case C1 and figure 13(e–h) for Case C2. The region in the lee of the ripple, where the main differences occur, is marked with red ellipses in the figures. We see that S^- in C1 follows a path closer to

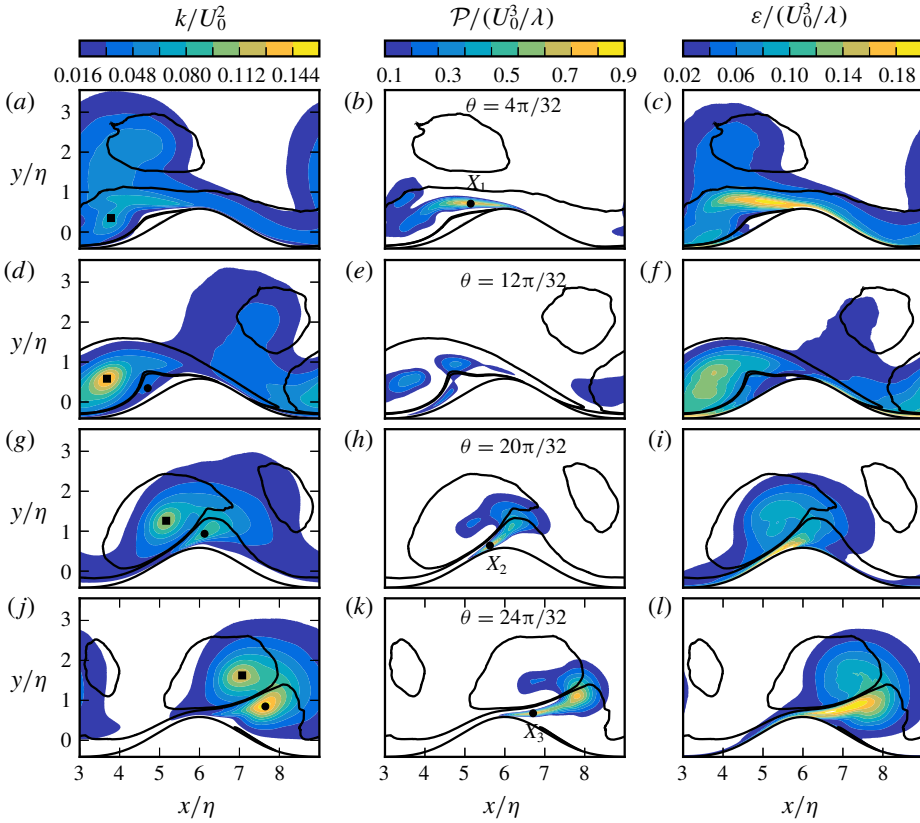


FIGURE 12. (Colour online) Evolution of TKE-budget terms in Case C2. See figure 11 for captions.

Cases	C1			C2		
	X_1	X_2	X_3	X_1	X_2	X_3
θ	$4\pi/32$	$20\pi/32$	$24\pi/32$	$4\pi/32$	$20\pi/32$	$24\pi/32$
$(x/\eta, y/\eta)$	(5.15, 0.67)	(5.85, 0.63)	(6.85, 0.54)	(5.15, 0.71)	(5.63, 0.64)	(6.71, 0.68)
$\ \mathbf{u}\ /U_0$	0.65	1.16	0.91	0.63	1.26	1.09
k/U_0^2	0.21	0.13	0.15	0.08	0.06	0.06
$\mathcal{P}/U_0^3\lambda$	3.12	1.67	1.99	0.82	0.84	0.89
\mathcal{P}/ε	5.1	4.89	5.61	4.52	5.19	4.97
$S/(U_0/\lambda)$	36.91	76.08	46.78	33.54	40.5	46.21
K	2.77	7.02	5.02	5.89	11.03	8
S^*	12.8	28.58	19.21	13.78	15.63	15.19
$ \Pi_b $	0.09	0.16	0.12	0.17	0.20	0.17
$ \Pi_v $	0.01	0.16	0.02	0.01	0.08	0.12

TABLE 4. Turbulence parameters at peak-production points for three representative phases. See (5.1)–(5.4) for the definitions of Π_b , Π_v , K and S^* .

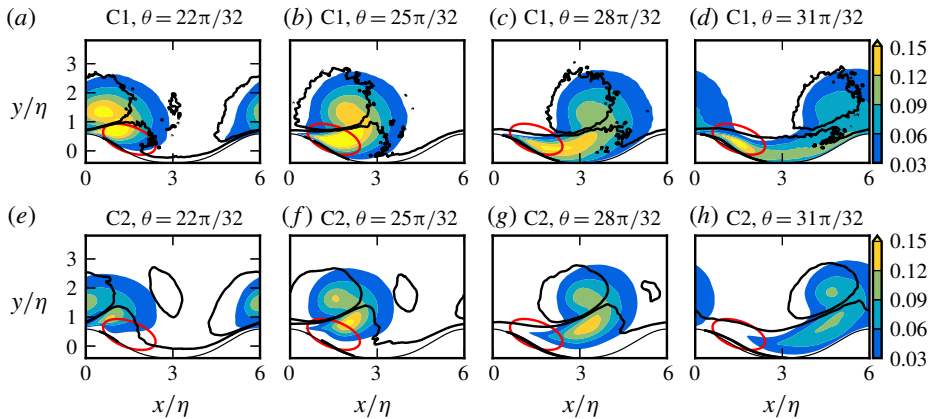


FIGURE 13. (Colour online) Filled contours showing the evolution of k/U_0^2 during the vortex-ejection (acceleration) stage. Contour lines indicate $|\langle \omega_z \rangle| = 0.15U_0/\eta$. (a–d) Case C1; (e–f) Case C2.

the ripple surface due to a more horizontal ejection angle. This leads to more intense vortex–wall interactions, which increase turbulence levels in the marked regions. In contrast, k remains low near the wall in C2, as S^- follows a higher trajectory limiting the wall interference. Consequently, the lee of the ripple remains quite turbulent in C1 during the passage of the vortices, and the free separated layer at $\theta = 31\pi/32$ feeds an already well-developed turbulent zone at the trail of the vortices, cf. marked region in figure 13(d). This is not the case in C2, where the lee side remains ‘quiet’ after the passage of vortices, cf. figure 13(h). These observations provide some insights into the role of the ejection angle in the significantly different lee side turbulence levels (figures 11a and 12a) and global production rates at the start of the cycle (figure 9).

5.2. Turbulence statistics along a set of trajectories

Turbulence characteristics of the flow can be further elucidated using the data along the trajectories at certain representative locations. To this end, we have selected three locations at each instant: the cores of the P^+ and S^- vortices, and the point where the production rate \mathcal{P} peaks. Table 5 presents the details of the trajectories formed from these points. We have seen in previous sections that the cores of coherent vortices are characterized by peak levels of phase-averaged spanwise vorticity and turbulent kinetic energy. Since the focus is on turbulence in this section, the vortex-core trajectories $x_P(\theta)$ and $x_S(\theta)$ are defined by tracking the points where k peaks in the vortex at each respective phase. We track the primary vortex P^+ in $4\pi/32 \leq \theta \leq 33\pi/32$, and the secondary vortex S^- in $12\pi/32 \leq \theta \leq 33\pi/32$. The selected range for S^- starts at a later phase, as S^- forms later than P^+ , when the latter becomes strong enough to induce a secondary separation on the wall. Note that these temporal ranges are merely selected to present dynamically more interesting phases, and they do not correspond to the lifetime of the vortices – vortices exist before and after the selected time intervals. The resulting vortex-core trajectories are shown in figures 15(f,l) and 16(f,l). Similarly, the production peaks are tracked in $12\pi/32 \leq \theta \leq 25\pi/32$. This range is selected to elaborate the dynamics in the near-wall layers, and the trajectory follows the wall-attached portions of the S^- vortex during its ejection over the ripple.

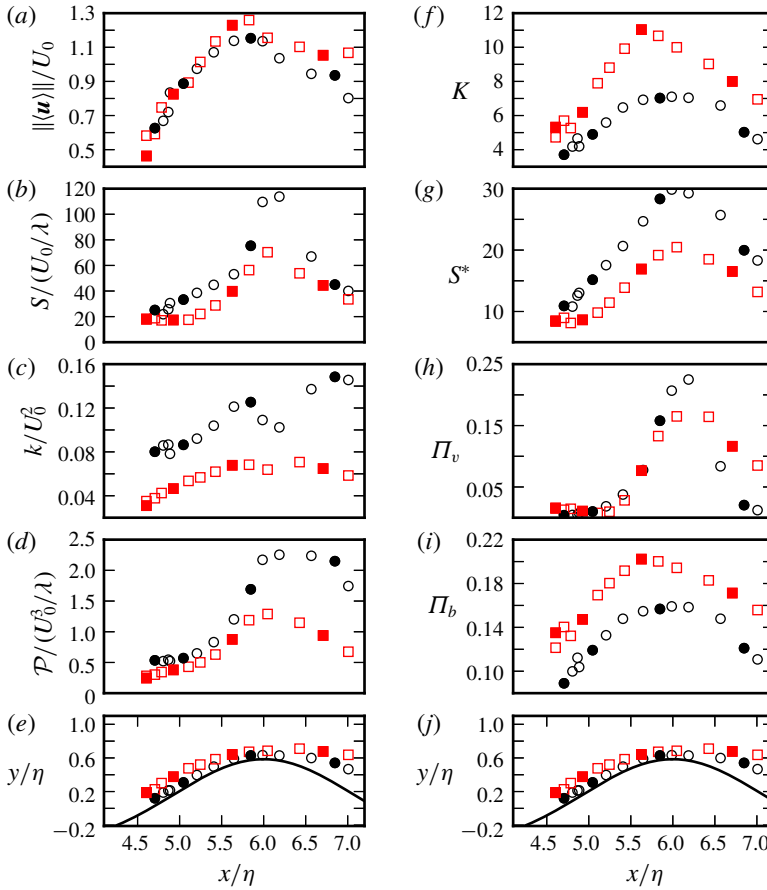


FIGURE 14. (Colour online) Evolution of flow quantities (a–d, f–i) along the production-peak trajectory $\mathbf{x}_k(\theta)$ (e,j) for $12\pi/32 \leq \theta \leq 25\pi/32$, cf. table 5. (O): Case C1; (□): Case C2. Each data point is separated in time by $\pi/32$, and filled markers indicate every fourth data point. See (5.1)–(5.4) for the definitions of Π_b , Π_v , K and S^* .

Trajectory	Phase location	Definition	Temporal range
$\mathbf{x}_P(\theta)$	Centre of P^+	$k(\mathbf{x}_P(\theta), \theta) \geq k(x, y, \theta)$ for $(x, y) \in P^+$	$4\pi/32 \leq \theta \leq 33\pi/32$
$\mathbf{x}_S(\theta)$	Centre of S^-	$k(\mathbf{x}_S(\theta), \theta) \geq k(x, y, \theta)$ for $(x, y) \in S^-$	$12\pi/32 \leq \theta \leq 33\pi/32$
$\mathbf{x}_k(\theta)$	Production peak	$\mathcal{P}(\mathbf{x}_k(\theta), \theta) \geq \mathcal{P}(x, y, \theta)$ for $(x, y) \in \Omega$	$12\pi/32 \leq \theta \leq 25\pi/32$

TABLE 5. Definition of two-dimensional trajectories employed in figures 14–16. The k -production trajectories \mathbf{x}_k are plotted in figure 14(e,j). Vortex-core trajectories \mathbf{x}_P and \mathbf{x}_S are plotted in figures 15(f,l) and 16(f,l).

The trajectory includes the points X_2 and X_3 from table 4. The point X_1 from the same table is not a part of the trajectory, as it is located in the free-shear layer feeding the P^+ vortex. Figure 14(e,j) shows the resulting peak-production trajectories $\mathbf{x}_k(\theta)$ for both cases.

Figure 14 demonstrates a set of turbulence parameters evaluated along the production trajectories (\mathbf{x}_k). We see that during the ejection phase, the S^- vortex accelerates towards the crest (figure 14*a*), and its wall-attached parts are highly stretched in this process, cf. the points in $5 \leq x/\eta \leq 6$ in figure 14(*b,g*). High straining, together with increasing turbulence levels (figure 14*c*), leads to a substantial rise in the production rate (figure 14*d*). The production rate reaches maximum levels near the crest, and starts to decay slowly after detachment of the vortex, cf. $x/\eta > 6$ in figure 14(*d*).

The turbulent fields at the production peaks show high anisotropy as they approach the crest, i.e. $5 \leq x/\eta \leq 6$, where K and the invariants of the anisotropy tensors increase substantially, cf. figure 14(*f,h,i*). The transition of the vorticity field from almost complete isotropy to high levels of anisotropy in $5 < x/\eta < 6$ is particularly remarkable, cf. figure 14(*h*). The invariants here peak at $\Pi_v \approx 0.25$ in C1, and $\Pi_v \approx 0.2$ in C2 – note that $\Pi_v = 1/3$ corresponds to the one-component limit of the anisotropy tensor. This growth in anisotropy suggests that coherent-vortex structures with a certain directional preference exist around the ripple crest in the range $20\pi/32 \leq \theta \leq 24\pi/32$. We will see in § 6 that these structures are counter-rotating vortex pairs that are elongated in the streamwise direction. In canonical near-wall turbulence, these coherent vortices are known to give rise to low streamwise-velocity streaks, as they lift up the low-momentum fluid between them (Swearingen & Blackwelder 1987; Robinson 1991). In this regard, the substantial increase in the anisotropy of the velocity field and K parameter in $5 < x/\eta < 6$ is consistent with the existence of streamwise vortices, cf. figure 14(*f,i*). After ejection from the crest, vorticity and velocity fields at the production peaks return to more isotropic states, cf. points for $x/\eta > 6$ in figure 14(*h,i*).

Figure 15 shows the evolution of turbulence parameters along the vortex-core trajectories $\mathbf{x}_p(\theta)$ (figure 15*a–e*) and $\mathbf{x}_s(\theta)$ (figure 15*g–k*). The vortex cores are also indicated in k plots of figures 11 and 12. We see in figure 15(*f,l*) that trajectories confirm the previous observations, as the $P^+–S^-$ vortex couple in C2 follows a higher altitude trajectory due to steeper ejection angle. Turbulent kinetic energy (k) and phase-averaged fluctuating enstrophy ($\mathcal{E} = \langle \omega_i' \omega_i' \rangle / 2$) in the P^+ -core are significantly higher in C1 than in C2 initially, cf. $x/\eta \approx 4$ in figures 15(*a,b*). There is a strong decay in k and \mathcal{E} in C1 afterwards. The vorticity is isotropic in the vortex cores of P^+ and S^- in C1, and almost isotropic in C2, cf. figures 15(*c*) and 15(*i*). This implies that small-scale motions reach locally isotropic states in coherent-vortex cores, so turbulence is well developed in these regions. We further see in figures 15(*e*) and 15(*k*) that the mean-shear parameters rise during the motion of the vortex couple towards the ripple crest, and they peak when the vortices pass the ripple crest (see the instance at $20\pi/32$ marked with green circles). This suggests that vortices strain each other by mutually induced velocity fields. Such a straining effect elucidates the elliptic deformations observed in § 3.

Higher-order moments, i.e. the skewness $\mathcal{S}(a) = \langle a^3 \rangle / \langle a^2 \rangle^{3/2}$ and the kurtosis $\mathcal{K}(a) = \langle a^4 \rangle / \langle a^2 \rangle^2$, of the fluctuating streamwise velocity u'_x and of its streamwise derivative $\partial u'_x / \partial x$ are shown in figures 16(*a–d*) and 16(*g–j*) along the $\mathbf{x}_p(\theta)$ and $\mathbf{x}_s(\theta)$ trajectories, respectively. Furthermore, the Taylor-microscale Reynolds number

$$Re_T = u' \lambda_T / \nu, \quad (5.5)$$

where $u' = \sqrt{2k/3}$ and $\lambda_T = \sqrt{10\nu k/\varepsilon}$, is also evaluated along the trajectories, cf. figures 16(*e*) and 16(*k*).

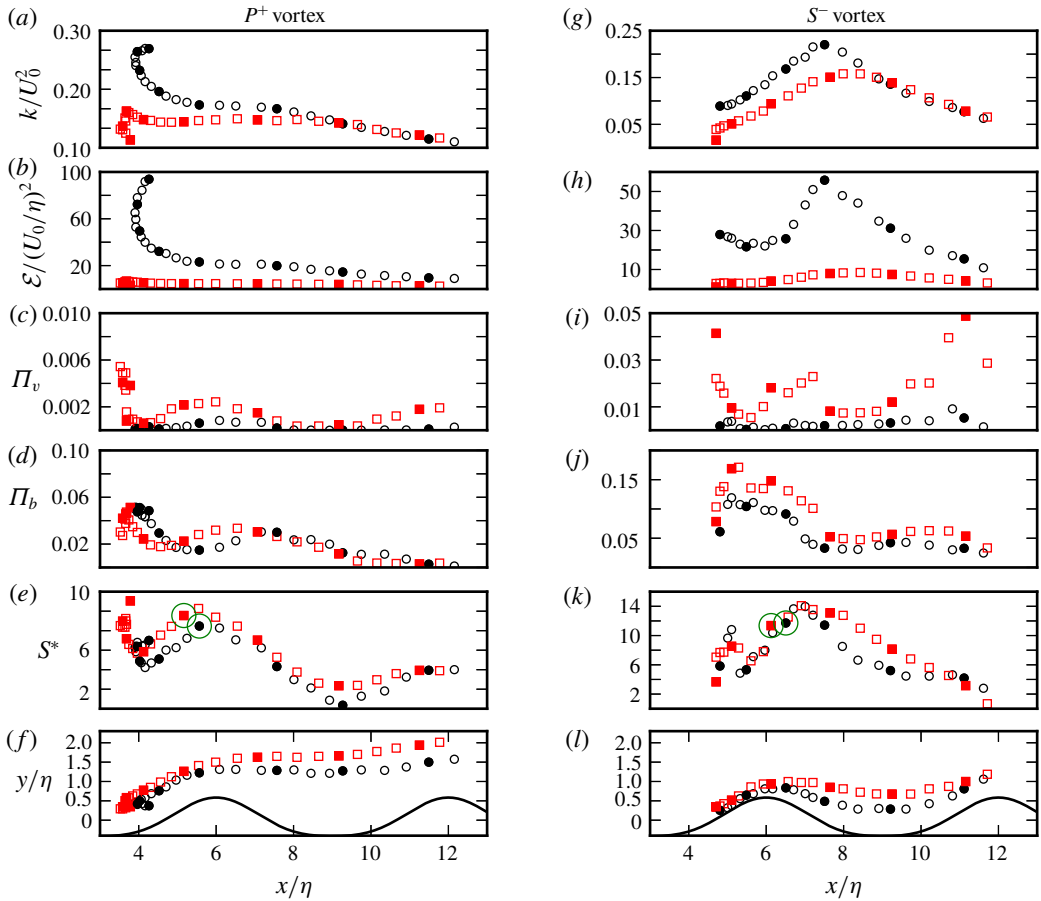


FIGURE 15. (Colour online) Trajectory of the (f) P -vortex cores ($\mathbf{x}_p(\theta)$) for $4\pi/32 \leq \theta \leq 33\pi/32$ and (l) S -vortex cores ($\mathbf{x}_p(\theta)$) for $12\pi/32 \leq \theta \leq 33\pi/32$, cf. table 5 for the definition of trajectories. Turbulence parameters evaluated (a–e): on $\mathbf{x}_p(\theta)$; (g–k): on $\mathbf{x}_s(\theta)$. (○): Case C1; (□): Case C2. Each data point is separated by $\pi/32$ in phase, and filled markers indicate every fourth data point. See (5.1), (5.2) and (5.4) for the definitions of Π_b , Π_v , and S^* .

Figures 16(a,c) and 16(g,i) show that the velocity derivatives deviate from Gaussianity ($\mathcal{S} = 0$, $\mathcal{K} = 3$ in a Gaussian distribution) in both vortex cores. The deviation is particularly strong in kurtosis, which is typical for developed turbulent flows due to their internal intermittency, as first observed by Batchelor & Townsend (1949). Experimental data showed a Reynolds number dependent variation $\mathcal{K}(\partial u'_x/\partial x) = Re_T^{3/8}$ for this departure (Van Atta & Antonia 1980). These variations are shown with solid lines in figures 16(a) and 16(g). We see that initially $\mathcal{K}(\partial u'_x/\partial x)$ in both vortex cores is consistent with experimental values, and follows the $Re_T^{3/8}$ -curves. The kurtosis dramatically increases then in C1 despite the decreasing Re_T , cf. $x/\eta > 6$ in figure 16(a,e) and $x/\eta > 8$ in figure 16(g,k). High values in the range of $\mathcal{K}(\partial u'_x/\partial x) \approx 15$ are reached, showing a stronger departure from Gaussianity than expected in standard fully developed turbulence. This suggests an additional

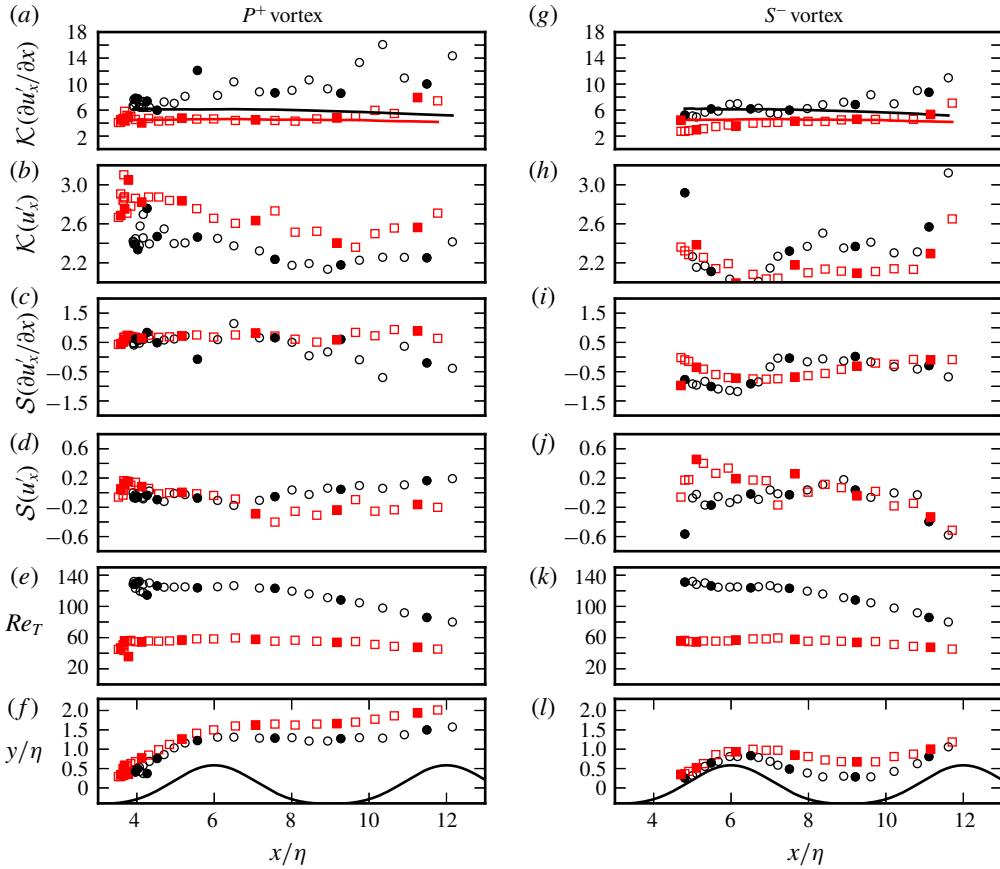


FIGURE 16. (Colour online) High-order moments (a–d) and (g–j) evaluated on $x_p(\theta)$ (f) for $4\pi/32 \leq \theta \leq 33\pi/32$ and on $x_s(\theta)$ (l) for $12\pi/32 \leq \theta \leq 33\pi/32$, cf. table 5 for the details about trajectories $x_p(\theta)$ and $x_s(\theta)$. The Taylor-microscale Reynolds number (5.5) evaluated on $x_p(\theta)$ (e) and on $x_s(\theta)$ (k). (○): Case C1; (□): Case C2. Each data point is separated by $\pi/32$ in time, and filled markers indicate every fourth data point. \mathcal{K} is the kurtosis, \mathcal{S} is the skewness.

intermittency mechanism on the spanwise-vortex column. We will see in § 6 that the spanwise vortices disintegrate into large-scale vortex clusters with relatively quiet regions in between, which is indicative of external intermittency. The vortices in C2 do not develop such a strong external intermittency, and the departures from experimental values of kurtosis are relatively modest.

Figures 16(b) and 16(h) further show that $\mathcal{K}(u'_x) < 3$ for all of the trajectories (except for some initial points of P^+ in C2). This shows that the probability density functions (PDFs) of the streamwise velocity are more flat than the normal distribution, i.e. high deviations from the mean value are rarer than for a random Gaussian variable. Furthermore, PDFs of the streamwise velocities are in general skewed. In particular, S^- -cores show pronounced negative skewness, when S^- arrives at the neighbouring ripple, cf. $x/\eta > 9$ in figure 16(j).

5.3. Statistics of the wall shear stress

A significant quantity for sediment-transport processes is the imposed shear stress on the ripple surface. In §3, we analysed a related quantity, i.e. the spanwise wall vorticity (cf. figure 6). The local phase-averaged tangential shear stress, simply the wall shear stress, on the ripple surface Ω_η can be calculated using the wall vorticity as follows

$$\langle \tau_t(\mathbf{x}, \theta) \rangle = -\nu \langle \omega_z(\mathbf{x}, \theta) \rangle \quad \text{for } \mathbf{x} \in \Omega_\eta. \quad (5.6)$$

Using the Reynolds decomposition, the instantaneous wall shear stress can be written as $\tau_t = \langle \tau_t \rangle + \tau'_t$, where τ'_t is the fluctuating part.

Figure 17 shows the distribution of the wall shear stress and its fluctuation intensity over the period. The values in figure 17(a,b) are normalized by $\tau_{max}^f = \rho U_0^2 Re^{-1/2}$, which is the maximum value for the wall shear stress in a laminar sinusoidal oscillatory flow over a flat smooth wall (Batchelor 2000). The laminar scaling is selected, as Reynolds numbers in this work are below the transition Reynolds number ($Re \approx 40\,000$, cf. Jensen, Sumer & Fredsoe (1989)) of the smooth bottom oscillatory boundary layer. The regions with intense shear are of most practical interest, as they imply regions prone to active sediment motion. In order to elaborate the statistics in these regions, we define a high-shear trajectory $\mathbf{x}_\tau(\theta)$, which goes through the phase maxima of the wall shear stress at the lee of the ripple. The thick solid lines in figure 17 show the evolution of the trajectory over the ripple for $0 \leq \theta \leq 40\pi/32$. The maximum shear on this trajectory occurs at $\mathbf{x}_\tau(22\pi/32)$ for both cases. This is the global maximum of the wall shear stress, which will be denoted as τ_{max} , i.e. $\tau_{max} := \max\{\langle \tau_t(\mathbf{x}, \theta) \rangle\}$ for $\mathbf{x} \in \Omega_\eta$. The intensities in figure 17(c,d) are normalized by these respective values of τ_{max} . Black markers in figure 17(a,b) indicate τ_{max} for both cases, where $\tau_{max} = 4.18\tau_{max}^f$ in Case C1 and $\tau_{max} = 1.08\tau_{max}^f$ in Case C2. We see an increase in the wall-shear-stress peak with increasing Re in contrast to laminar oscillatory boundary layers over a smooth flat wall, where wall shear stress decays with $Re^{-1/2}$.

At the start of the period in $0 \leq \theta \leq 26\pi/32$, $\langle \tau_t(\mathbf{x}_\tau(\theta), \theta) \rangle$ corresponds to the footprint of the P^+ -vortex that is forming and will eventually eject itself in the positive streamwise direction. The relation of these intense shear locations to the motion of the vortex was discussed in §3; $\langle \tau_t \rangle$ reaches its highest values in the range $16\pi/32 \leq \theta \leq 36\pi/32$ near the ripple crest, cf. figure 17(a,b). Two peaks are observed in this range. The first one is τ_{max} at $\theta = 22\pi/32$ and occurs during the ejection of the vortex pair from the crest. The second peak occurs at $\theta \approx \pi$, when the free-stream velocity peaks. It is observed that high fluctuation regimes occur near these peaks, cf. figure 17(c,d). The intensities in figure 17(c,d) are normalized by these respective values of τ_{max} .

Figure 18 shows the statistical moments of τ_t on high-shear trajectories $\mathbf{x}_\tau(\theta)$. Two regimes with high $\langle \tau_t \rangle$ and $\langle \tau_t^2 \rangle$ appear as two peaks after $\theta > 16\pi/32$, cf. figure 18(a,b). The flatness factors (figure 18c) and the skewness factors (figure 18d) show that these two intense shear regimes have very different fluctuation characteristics. There is a dramatic rise in the skewness and flatness in the second high-stress regime, which takes place at approximately $27\pi/32 < \theta < 34\pi/32$. This rise, occurring slightly ahead of the rise in the first- and second-order moments, leads to strong departures from a normal distribution in the PDFs, $f(\tau_t)$. This is shown in figure 19 using PDFs at two different phases: an instance in the vortex-ejection regime at $\mathbf{x}_\tau(20\pi/32)$ and another instance in the high free-stream velocity regime at $\mathbf{x}_\tau(31\pi/32)$. These selected points on \mathbf{x}_τ are indicated by the green markers in figure 17. We see that the PDFs at $\theta = 31\pi/32$ show high positive skewness with long tails, so the mean values do not have the highest probability density.

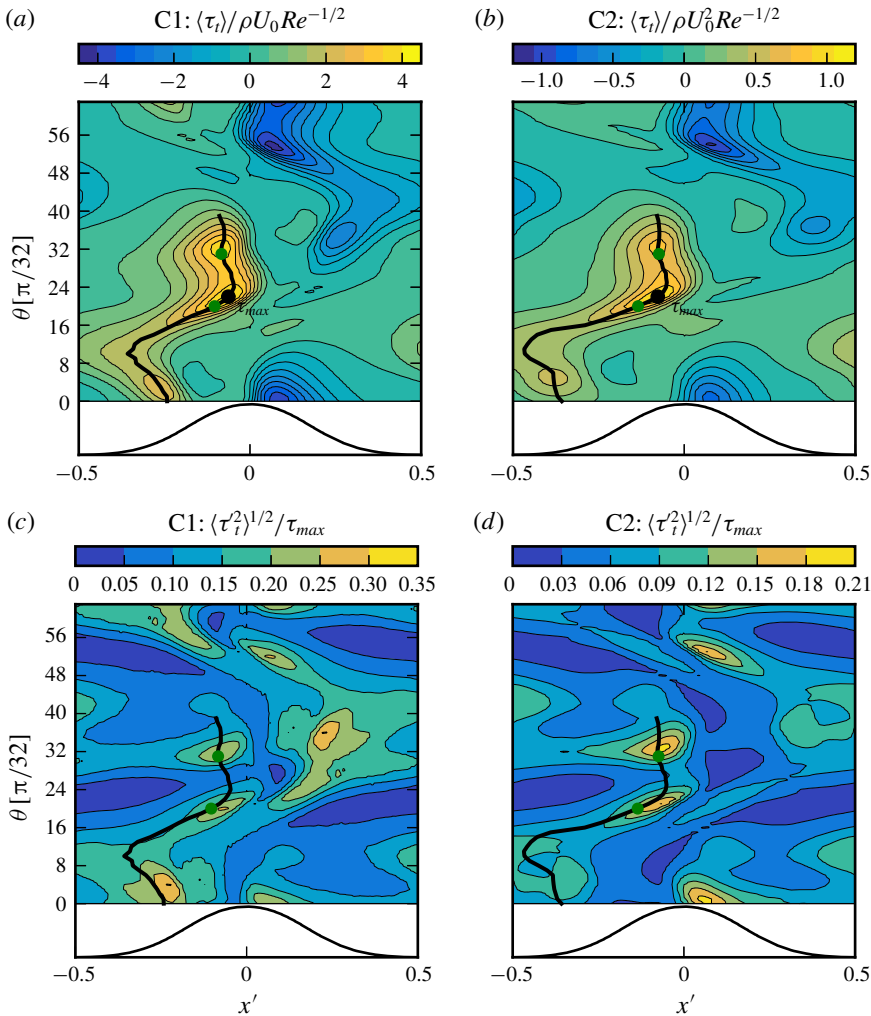


FIGURE 17. (Colour online) Distribution of the phase-averaged wall shear stress $\langle \tau_t \rangle$ (a,b) and its fluctuation intensity $\langle \tau_t'^2 \rangle^{1/2}$ (c,d). The location of the global maximum of the wall shear stress, i.e. $\tau_{max} := \max\{\langle \tau_t(\mathbf{x}, \theta) \rangle\}$, is indicated by the black markers in (a,b). The intensities are normalized by this value in the respective cases. The thick solid lines go through the phase maxima of the local wall shear stress. The probability density functions of τ_t at the locations shown with green markers are plotted in figure 19.

The strongly non-Gaussian range in $27\pi/32 < \theta < 34\pi/32$ is related to the passage of the $P^+ - S^-$ vortices from the previous half-cycle over the ripple crest. Therefore, the positively skewed fluctuations with long tails appear to be imposed by these vortices.

6. Three-dimensional structures

The main structural elements of the flow are the coherent spanwise vortices whose two-dimensional phase-averaged statistics were studied in the previous sections. The observations in § 5.2 suggested that these vortices lose their spanwise coherence and would develop external intermittency. Furthermore, the resulting intermittent features

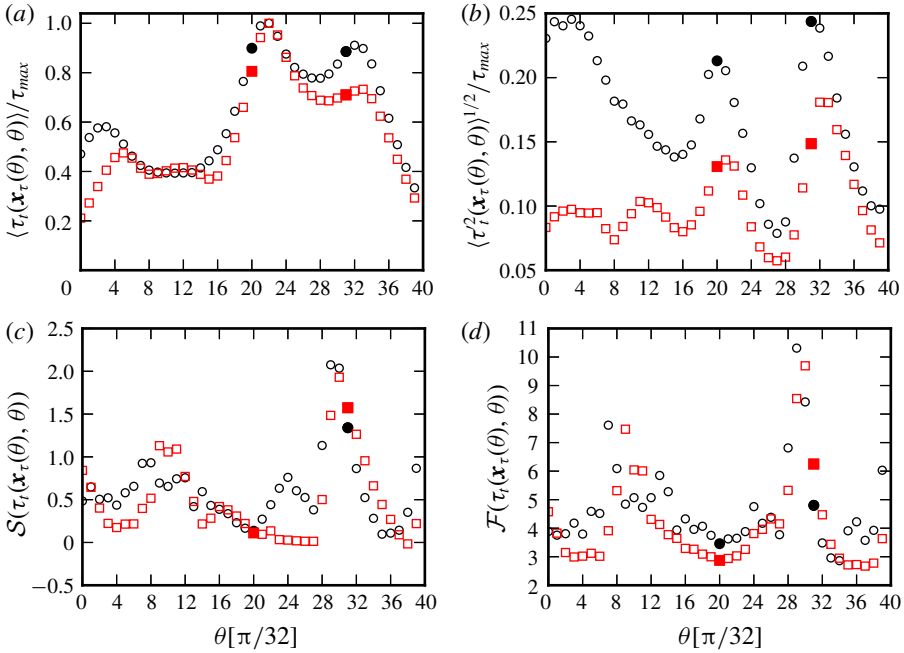


FIGURE 18. (Colour online) Central moments of the wall shear stress evaluated on a high-shear trajectory $\mathbf{x}_\tau(\theta)$, cf. thick lines in figure 17. (a) Mean value scaled with $\tau_{max} := \max\{\langle \tau_t(\mathbf{x}, \theta) \rangle\}$; (b) fluctuation intensity scaled with τ_{max} ; (c) the skewness factor $\mathcal{S}(\tau_t') = \langle \tau_t'^3 \rangle / \langle \tau_t'^2 \rangle^{3/2}$; (d) the flatness factor $\mathcal{F}(\tau_t') = \langle \tau_t'^4 \rangle / \langle \tau_t'^2 \rangle^2$. (○) Case C1; (□) Case C2. The filled markers indicate the selected phases for the presentation of PDFs in figure 19.

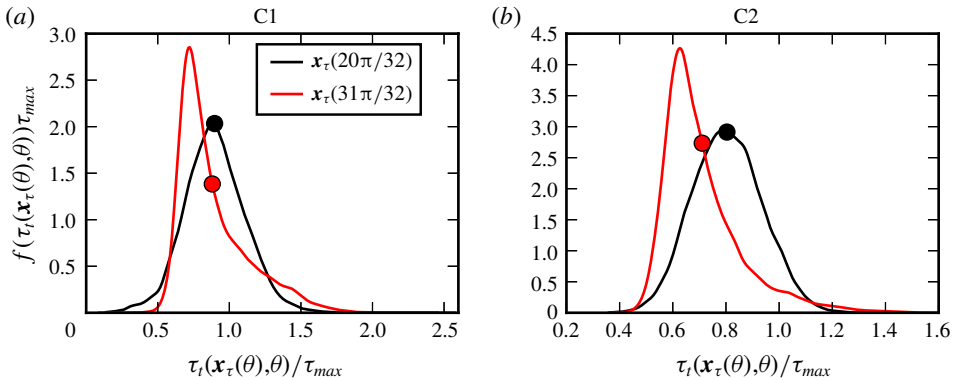


FIGURE 19. (Colour online) Probability density functions (PDFs) of the local wall shear stress, $f(\tau_t)$, evaluated at $\mathbf{x}_\tau(20\pi/32)$ and $\mathbf{x}_\tau(31\pi/32)$. The selected points are indicated with green markers in figure 17. Markers show the PDFs of mean values, i.e. $f(\langle \tau_t(\mathbf{x}_\tau(\theta), \theta) \rangle)$. Sample spaces are normalized with the global maximum of the wall shear stress, i.e. $\tau_{max} := \max\{\langle \tau_t(\mathbf{x}, \theta) \rangle\}$, cf. black markers in figure 17(a,b).

appear to have an influence on the non-Gaussian wall-shear-stress fields when they arrive at the neighbouring ripple. In this section, we provide visual evidence for these results, and also conduct further statistical analyses using the transverse spectra of the

fluctuating fields along the vortex trajectories. To this end, we focus on the energetic vortex modes responsible for the breakdown of spanwise coherence. We have further observed in § 5.2 (cf. figure 14*g,h*) that anisotropies in the fluctuating fields increase drastically in the near-wall region when the P - S dipole moves over the crest. This suggested that coherent structures with strong alignment to one direction dominate the near-wall layer in this phase. We will also study these near-wall turbulent structures and their footprints on wall-shear-stress fluctuations.

6.1. Three-dimensional visualization of instantaneous flow fields

We start our analysis with three-dimensional visualizations of the instantaneous flow. Only the fluctuating fields are considered, as we have discussed the motion of Reynolds-averaged fields in detail in § 3. We focus on the ejection phase ($\theta \geq \pi/2$). The spanwise vortices in the vortex-formation phase ($\theta < \pi/2$) remain relatively immobile at the lee side, and their footprints on the ripple surface are mild until their ejection over the ripple (cf. the discussion in § 5.3). Therefore, their structural features in the vortex-formation phase are of less importance, and are not presented here for brevity. A more complete picture including the vortex-formation phase will be given in the spectral analysis of § 6.2.

In order to extract the flow structures, we employ the second invariant of the fluctuating velocity gradient tensor, i.e.

$$Q = \frac{1}{2}(\Omega'_{ij}\Omega'_{ij} - s'_{ij}s'_{ij}), \quad (6.1)$$

where $\Omega'_{ij} = 1/2(\partial u'_i/\partial x_j - \partial u'_j/\partial x_i)$ is the fluctuating rate of spin tensor. The Q -invariant extracted from fluctuating fields is usually employed to analyse inhomogeneous turbulent flows, e.g. Gomes-Fernandes, Ganapathisubramani & Vassilicos (2014) and Buxton, Breda & Chen (2017). Positive values of Q occur in the regions where the fluctuating vorticity dominates over the fluctuating strain. These regions are intense in enstrophy. Similarly, negative values of Q occur in strain-dominated regions, which are strongly dissipative. Both strain and vorticity are essential in the turbulent dynamics, as the term $\omega'_i\omega'_j s'_{ij}$ is the main driver of the enstrophy production and the turbulent cascade (Tennekes & Lumley 1972). We have observed in our simulations that large values of positive and negative Q concentrate in the same regions. Therefore, we use merely the positive isosurfaces of Q to visualize dynamically active regions. The regions of intense strain usually neighbour the visualized regions, and are not discussed below for brevity.

Figure 20 demonstrates intensive enstrophy regions in a selected subdomain for three different phases at $\theta = 20\pi/32, 26\pi/32, 31\pi/32$. The isosurfaces are coloured with the fluctuating streamwise velocity u'_x . We see that during their ejection from the crest at $\theta = 20\pi/32$, the P^+ and S^- vortices are in the form of turbulent vortex clouds that span the entire lateral dimension of the selected subdomain (also of the entire computational domain, not shown here), cf. figure 20(*a,b*). In C1, there are large regions on the vortex cloud that are predominantly in red, i.e. have a higher velocity than its surrounding. These regions indicate the presence of an unstable vortex mode on the vortex column, which gives rise to large-scale high-momentum structures with spanwise dimensions of approximately $3\eta - 4\eta$. One instance of these high-momentum structures is marked with a black circle in figure 20(*a*). These structures cannot be easily identified in C2 with the selected visualization method. However, we will see in spectral analysis in § 6.2 that a dominant vortex mode also exists in C2.

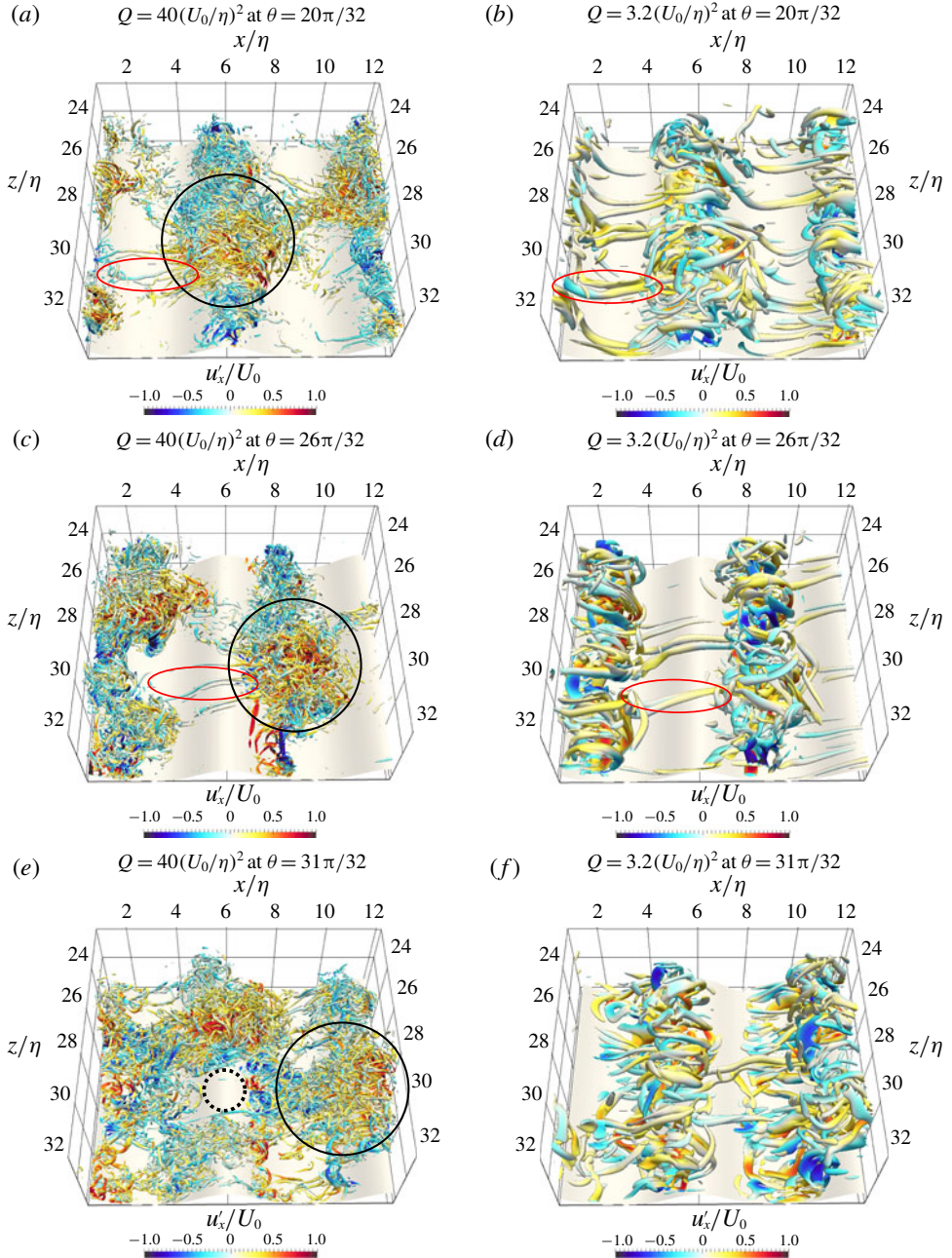


FIGURE 20. (Colour online) Isosurfaces of Q parameter (cf. (6.1)) at three different instances $\theta = 20\pi/32, 26\pi/32, 31\pi/32$. Surfaces are coloured based on streamwise-velocity fluctuations u'_x . The flows are convected from left to right. (a,c,e) Case C1, $Q = 40(U_0/\eta)^2$; (b,d,f) Case C2, $Q = 3.2(U_0/\eta)^2$. Black circles in (a,c,e) show the evolution of a high-momentum structure. Red ellipses in (a–d) indicate an instance of streamwise-oriented vortical structures.

In addition to large-scale momentum structures on the vortex column, there are also organized features near the wall in the form of streamwise-oriented elongated vortex pairs. Two examples are indicated with red ellipses in figure 20(a,b). In C2, these vortices are arranged in a somewhat regular fashion along the entire spanwise extent (figure 20b). In contrast, in C1 they concentrate preferably in the trail of high-momentum structures (figure 20a). These streamwise-aligned longitudinal structures are responsible for the highly anisotropic near-wall layers observed in the statistical analysis of § 5.2 (cf. figure 14g,h).

When the coherent spanwise vortices detach themselves from the ripple crest, the streamwise structures are still observable in their trail around the crest, cf. red ellipses at $\theta = 26\pi/32$ in figure 20(c,d). We further see in this phase that the high-momentum structure (black circle) in C1 keeps its coherence, whereas low-momentum regions (blue parts) around it become slowly depleted in intense vortical structures.

Figure 20(e,f) show the phase $\theta = 31\pi/32$ when the vortex clouds arrive at the crest of the neighbouring ripple. These structures show quite different characteristics in C1 and C2. We see in figure 20(e) that vortical structures in C1 survive only in the regions with high fluctuating velocity (marked with solid circle) and are mostly depleted in low velocity regions (marked with dotted circle). As the regions between high-momentum structures are relatively quiet in terms of intense vortical structures and strain structures (not shown here), the flow can be considered intermittent in the spanwise direction. Namely, small-scale turbulence preferentially concentrates in regions with positive fluctuating velocity. We denote the final isolated form of the high-momentum structure as a turbulent vortex cluster. Turbulent vortex clusters seem to have the tendency to be arranged in staggered patterns, such that there is a spanwise shift between the neighbouring vortex clusters in the streamwise direction. Such an arrangement is reminiscent of a brick pattern. The clustering of highly vortical elements in high-momentum structures is not observed in C2 (figure 20f). These observations provide a visual perspective for the relatively high kurtosis in the velocity derivative $\partial u_x'/\partial x$ (a small-scale quantity like Q) compared with the standard values in fully developed turbulence at vortex cores of C1 (cf. figures 16.Ia and 16.IIa). As the external intermittency is not strong in C2, the small-scale kurtosis in C2 remains close to fully developed turbulence values, cf. the discussion in § 5.2.

Large-scale momentum structures have strong footprints on the wall. This is shown in figure 21 for Case C1 at phases $\theta = 20\pi/32, 31\pi/32$. These phases are in the regimes where the peak values of wall shear stress and its fluctuation occur (cf. figure 17a,c). The dotted lines in figure 21(a,c) indicate the locations on the ripple where the phase-averaged wall shear stress peaks at the respective phase, i.e. $x_\tau(20\pi/32)$ and $x_\tau(31\pi/32)$ (cf. the green markers in figure 17a). It is observed at $\theta = 20\pi/32$ that wall-shear-stress fluctuations closely follow the large-scale patterns in the spanwise vortex. One instance of this relation is marked with circles in figure 21(a,b). A high shear-stress region with circa $3\eta - 4\eta$ width is observed in figure 21(a), which is at the footprint of a high-momentum structure indicated in figure 21(b). Furthermore, the selected high-stress region also features narrow stripy patterns elongated in the streamwise direction, which are produced by near-wall streamwise vortices and accompanying low-speed streaks.

At $\theta = 31\pi/32$, turbulent vortex clusters sweep the neighbouring ripple and induce large-scale fluctuations in wall shear stress in this process. One instance of this event is indicated with circles in figure 21(c,d). The induced fluctuations due to sweeping are significantly more intense than the ones observed during the ejection of the vortex cloud (note the different range employed in colour bars of figure 21a,c). Outside the

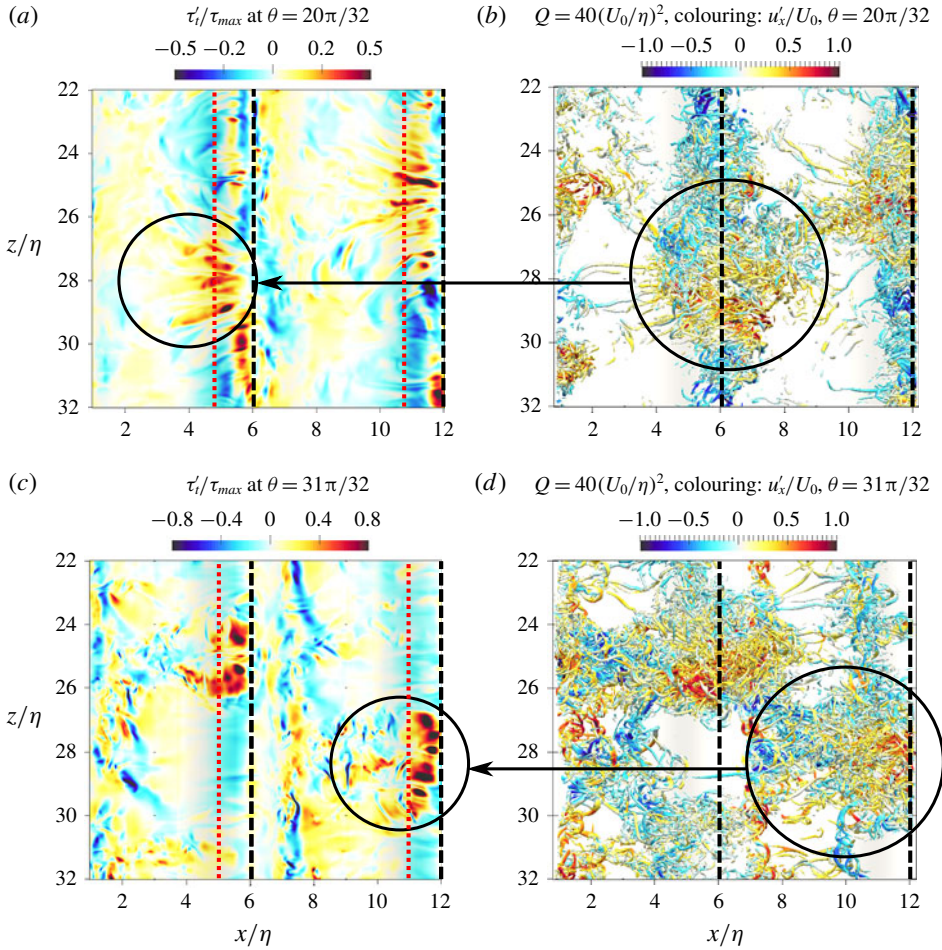


FIGURE 21. (Colour online) Footprints of turbulent vortex clusters on the wall shear stress for Case C1. (a,c) Wall-shear-stress fluctuations τ'_i/τ_{max} ; (b,d) top view of Q -isosurfaces coloured with streamwise-velocity fluctuations u'_x . Circles in (a,b) and (c,d) mark a large-scale structure and its footprint on the wall shear stress. Dashed lines show the ripple crests, and dotted lines in (a,c) show the location of maximum phase-averaged wall shear stress ($\langle \tau_i \rangle$).

contact regions with the vortex cluster, the shear-stress fluctuations appear negative and relatively weak.

We now turn to instantaneous signals along a spanwise line to further elaborate the vortex–wall interaction during the sweeping process. To this end, figure 22 shows in (a,b) the spanwise distributions of fluctuating streamwise velocity u'_x at the centre of the primary and secondary vortices ($\mathbf{x}_p(31\pi/32)$ and $\mathbf{x}_s(31\pi/32)$), and in (c) the wall-shear-stress fluctuations τ'_i on the high-shear line at the footprint of these vortices at $\mathbf{x}_\tau(31\pi/32)$, cf. the dotted line at $x/\eta \approx 11$ in figure 21(c). The selected points for probing, i.e. $\mathbf{x}_p(31\pi/32)$, $\mathbf{x}_s(31\pi/32)$ and $\mathbf{x}_\tau(31\pi/32)$, are shown in the inset in figure 22. The window corresponding to the marked vortex cluster and its footprint in figure 21(c,d) are encircled with green lines. It is observed in figure 22(c) that $\tau'_i(\mathbf{x}_\tau(31\pi/32), z, 31\pi/32)$ is highly intermittent and positively skewed. This is

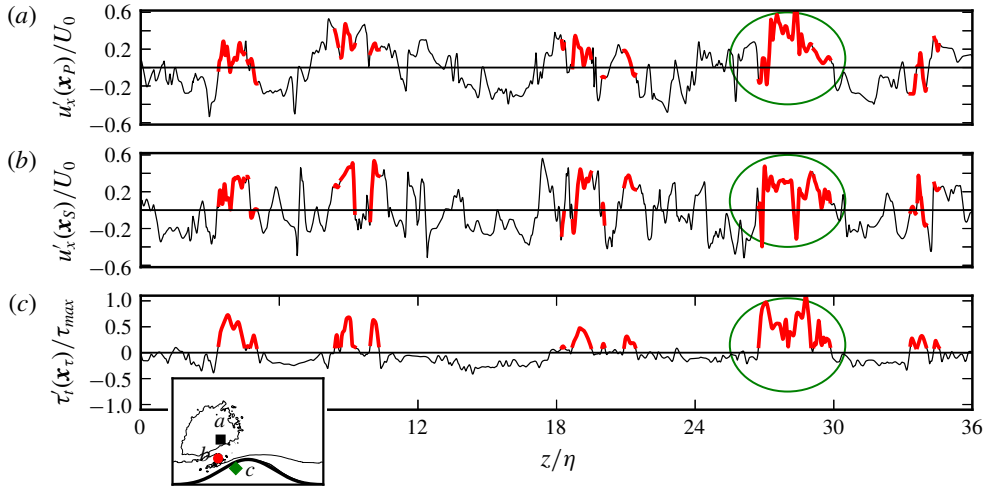


FIGURE 22. (Colour online) Instantaneous signals on the spanwise line at three selected locations at phase $31\pi/32$. (a) Streamwise velocity at the primary vortex core, $u'_x(\mathbf{x}_p(31\pi/32), z, 31\pi/32)$; (b) streamwise velocity at the secondary vortex core, $u'_x(\mathbf{x}_s(31\pi/32), z, 31\pi/32)$; (c) tangential wall-shear-stress fluctuations at the peak-stress point, $\tau'_t(\mathbf{x}_\tau(31\pi/32), z, 31\pi/32)$. The probing locations \mathbf{x}_p , \mathbf{x}_s and \mathbf{x}_τ are shown in the inset located at bottom left. The windows corresponding to the selected high-momentum vortex cluster in figure 21(c,d) are encircled with green lines. The red lines show the signals when $\tau'_t > 0.1\tau_{max}$.

the representation of the strongly non-Gaussian character of $\tau'_t(\mathbf{x}_\tau(31\pi/32), z, 31\pi/32)$ previously presented in figure 19(a).

We further see in figure 22 that positive values of τ'_t usually occur when the streamwise velocities are positive in the vortex cores. This is shown by marking the signals when $\tau'_t > 0.1\tau_{max}$, cf. the red lines. Here we selected $\tau'_t = 0.1\tau_{max}$ as a threshold to filter out weak positive fluctuations. A conditional average on these marked portions yielded $\langle u'_x(\mathbf{x}_p) |_{\tau'_t > 0.1\tau_{max}} \rangle / \langle u'_x(\mathbf{x}_p)^2 \rangle^{1/2} \approx 0.88$ and $\langle u'_x(\mathbf{x}_s) |_{\tau'_t > 0.1\tau_{max}} \rangle / \langle u'_x(\mathbf{x}_s)^2 \rangle^{1/2} \approx 0.74$. These values are remarkably high considering that the vortex cores are quite remotely located from the wall probe. Especially, the P^+ -core is located around η away from the wall. These strong correlations between the velocities in the vortex cores and the intermittent fluctuations in the wall shear stress are the manifestation of the sweeping mechanism observed in figure 21(c,d).

Wall shear stress is the driving force for mobilizing sediment grains or producing near-bed sediment transport (conventionally called bedload transport), so the spanwise fluctuation of wall shear stress can lead to spanwise inhomogeneity in sediment motion and eventually lead to spanwise variation of bed morphology. Our DNS simulations do not consider a mobile sand bed, but we still can expect that the spanwise inhomogeneity of wall shear stress should be equally or even more significant over real sand ripples. As a result, long-crested (two-dimensional) sand ripples are unstable and becomes three-dimensional eventually, which is observed in many laboratory experiments (e.g. O'Donoghue *et al.* 2006). Additional modelling work which includes sediment transport is required to further elucidate this hypothesis.

6.2. Analysis of spanwise spectra

We now turn to the spanwise spectral densities to analyse the average spanwise spacings of the observed structures in § 6.1. The spanwise spectral density function for fluctuating velocities is defined as follows

$$E_{ij}(\kappa_z, x, y, \theta) = \frac{1}{\Delta\kappa_z} \langle \hat{u}'_i(\kappa_z, x, y, \theta) \hat{u}'_j{}^*(\kappa_z, x, y, \theta) \rangle, \quad (6.2)$$

where \hat{u}'_i are the Fourier coefficients of the fluctuating velocity, cf. (2.7), $\hat{u}'_i{}^*$ are the complex conjugates, κ_z is the wavenumber in the spanwise direction and $\Delta\kappa_z = 2\pi/L_z$ is the wavenumber spacing. We will investigate the streamwise turbulent kinetic energy spectrum E_{xx} , where the integrated spectrum gives the streamwise turbulent kinetic energy, i.e. $\langle u'_x u'_x \rangle = \sum_{\kappa_z} E_{xx}(\kappa_z) \Delta\kappa_z$. Similarly, we define a spectral density function for the fluctuating vorticity

$$\Phi_{ij}(\kappa_z, x, y, \theta) = \frac{1}{\Delta\kappa_z} \langle \hat{\omega}'_i(\kappa_z, x, y, \theta) \hat{\omega}'_j{}^*(\kappa_z, x, y, \theta) \rangle, \quad (6.3)$$

where $\hat{\omega}'_i$ are the Fourier coefficients of the fluctuating vorticity. The spectrum of total enstrophy fluctuations is given by $\Phi_{\mathcal{E}} = \Phi_{ii}/2$, where repeated indices are summed. We consider this enstrophy spectrum to study the dissipative scales of motion. Finally, the spectral density for wall-shear-stress fluctuations is given by

$$T_{ij}(\kappa_z, x, y, \theta) = \frac{1}{\Delta\kappa_z} \langle \hat{\tau}'_i(\kappa_z, x, y, \theta) \hat{\tau}'_j{}^*(\kappa_z, x, y, \theta) \rangle, \quad (6.4)$$

where $\hat{\tau}'_i$ are the Fourier coefficients of the fluctuating wall-shear-stress component. We will consider only the spectrum of shear-stress fluctuations that are streamwise tangent to the ripple surface, i.e. T_{ii} .

The extracted spectral densities from our database contained a high noise-to-signal ratio due to limited sampling. In order to enhance the presentation, we have smoothed the data using the SciPy implementation of the Savitzky–Golay filter (Savitzky & Golay 1964). In this process, we employed second-order polynomials with a window length of nine samples. The raw spectra are shown in some of the figures for reference.

Figure 23 shows the premultiplied spectral densities $\kappa_z E_{xx}$ (lines) and $\kappa_z \Phi_{\mathcal{E}}$ (shades) along the vortex-core trajectories $\mathbf{x}_P(\theta)$ and $\mathbf{x}_S(\theta)$. A premultiplied spectral density plot shows the energy per $\log \kappa_z$, or $\log \lambda_z$. To show this, we first write the total energy using continuous variables $\langle u'_x u'_x \rangle = \sum E_{xx} \Delta\kappa_z \approx \int E_{xx} d\kappa_z$. In a log–linear plot with a logarithmic axis of wavenumbers, the integral reads $\int E_{xx} d\kappa_z = \int \kappa_z E_{xx} d \log \kappa_z$, where we have used $d\kappa_z = d \log \kappa_z / \kappa_z$. Finally, wavenumbers and wavelengths can be interchanged without modifying the integrand, as $d \log \kappa_z = -d \log \lambda_z$, i.e. $\int_{\kappa_{min}}^{\kappa_{max}} \kappa_z E_{xx} d \log \kappa_z = -\int_{\lambda_{max}}^{\lambda_{min}} \kappa_z E_{xx} d \log \lambda_z = \int_{\lambda_{min}}^{\lambda_{max}} \kappa_z E_{xx} d \log \lambda_z$. In the premultiplied spectrum plots, equal areas indicate equal contributions to energy. Premultiplied spectral density analysis is commonly employed to identify energetic turbulent structures in regions with intense multiscale dynamics, e.g. outer layer of wall-bounded flows (Hutchins & Marusic 2007; Jiménez 2013).

We see in figure 23 that contour lines and shaded contours minimally overlap in C1 (figure 23*a,b*), while they share most of the spectrum in C2 (figure 23*c,d*). Namely, the dissipative (enstrophy-containing) and energy-containing scales are well separated in

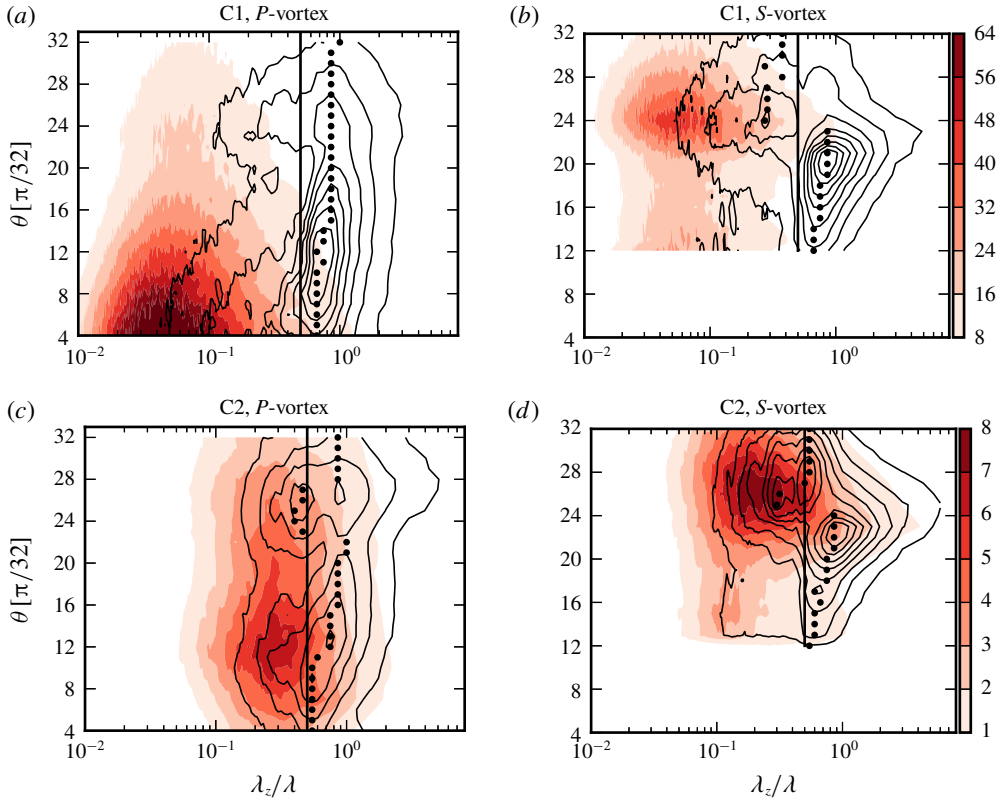


FIGURE 23. (Colour online) Premultiplied one-dimensional spectra of streamwise turbulent kinetic energy ($u'_x u'_x$) and enstrophy (\mathcal{E}) evaluated for spanwise wavelengths along the vortex-core trajectories $\mathbf{x}_P(\theta)$ and $\mathbf{x}_S(\theta)$, cf. table 5 for the definition of trajectories. (a,c) *P*-vortex, i.e. $\kappa_z E_{xx}(\kappa_z, \mathbf{x}_P(\theta), \theta)/U_0^2$ (contours) and $\kappa_z \Phi_\varepsilon(\kappa_z, \mathbf{x}_P(\theta), \theta)/(U_0/\eta)^2$ (shades). (b,d) *S*-vortex, i.e. $\kappa_z E_{xx}(\kappa_z, \mathbf{x}_S(\theta), \theta)/U_0^2$ (contours) and $\kappa_z \Phi_\varepsilon(\kappa_z, \mathbf{x}_S(\theta), \theta)/(U_0/\eta)^2$ (shades). (a,b) Case C1, contour levels are 0.04(0.04)0.32; (c,d) Case C2, contour levels are 0.025(0.025)0.2.

C1, as the former occurs on substantially smaller scales. Saffman (1978) suggested a well-defined separation between the energy-containing range and the dissipative range when the Taylor-microscale Reynolds number exceeds a critical value $Re_T^c \approx 100$. Our results are consistent with Saffman’s conjecture, as $Re_T > Re_T^c$ along \mathbf{x}_P and \mathbf{x}_S in the case of C1, and $Re_T \approx 60$ in the case of C2 (cf. figures 16e and 16j). Dimotakis (2000) further showed that many turbulent flows change their dynamics and qualitative behaviour when their Reynolds number is above Re_T^c . He defined this second step of transition (after the breakdown of the laminar state) as the mixing transition, since the flows possess significantly enhanced and more homogeneous mixing properties following this transition. Beyond the mixing transition, general flow properties appear to be only weakly dependent on the Reynolds number, hence the turbulence can be assumed to be fully developed. In this regard, the flow in C1 is in a fully developed post-mixing-transition state. Marked differences in the instantaneous snapshots (figure 20) and big disparity in the enstrophy levels of the cases (cf. e.g. figures 15b and 15g) can be attributed to this fact.

We now turn to the spectral distribution of the streamwise turbulent kinetic energy along the trajectories of the vortex cores. The peaks in the spectra at each phase are marked with dots in figure 23. It is observed in figure 23(a) that the energy in P -vortex cores initially centred around a peak at $\lambda_z \approx 0.6\lambda$ in Case C1. The energetic centre slowly evolves to $\lambda_z \approx 0.9\lambda$ and remains dominant throughout the remaining lifetime of the vortex. This high concentration of energy in certain wavelengths is the manifestation of a dominant vortex mode. This mode is responsible for breaking down coherent spanwise vortices into intermittent vortex clusters in C1, cf. § 6.1. The wavelengths of the peaks represent the average spanwise spacing for large-scale structures observed in figure 20(a,c,e) and figure 21(b,d). A similar energetic vortex mode is also observed in the P -vortex cores of Case C2, cf. figure 23(c). The growth of the mode in both cases, i.e. the increase of the wavelengths from $\lambda_z \approx 0.6\lambda$ to $\lambda_z \approx 0.9\lambda$, suggests merging of some neighbouring structures during the evolution of the coherent vortex.

Figure 23(b,d) shows that the energetic vortex mode is also effective in the S -vortices. It becomes increasingly prominent in the spectra when the vortex moves towards the crest in the self-ejection process in the range $12\pi/32 \leq \theta \leq 20\pi/32$. The energy of the mode reaches a global peak around $\theta = 20\pi/32$, i.e. just before the ejection of the vortex from the crest. We see that after the ejection, the portion of the vortex mode in S -vortex is demolished, and energy concentrates in smaller wavelengths, cf. $\theta > 24\pi/32$ in figure 23(b,d). We also note that after ejection from the wall, the enstrophy significantly increases in the S -vortex core, cf. the rise in the shaded contour levels in figure 23(b,d). This suggests a transition to a more dissipative and less coherent state, under which small-scale motions are promoted.

The overall dominance of the vortex mode can be elaborated using the cumulative energy contribution of the spectral range related to this mode. Such a cumulative analysis, where a certain range of scales is attributed to a class of turbulent structures, has been previously employed to investigate the prominence of flow structures in turbulent wall-bounded flows, cf. e.g. Guala, Hommema & Adrian (2006). To this end, the fraction of the fluctuation energy in the wavelengths greater or equal than a selected wavelength λ_c is calculated with

$$\mathcal{Y}_{ij}(\lambda_c) = \frac{\sum_{\kappa_z=0}^{\kappa_z=2\pi/\lambda_c} E_{ij}(\kappa_z)}{\sum_{\kappa_z=0}^{\kappa_z=\kappa_z^{max}} E_{ij}(\kappa_z)}. \quad (6.5)$$

We omitted the explicit dependency of E_{ij} on y, z, θ for brevity. To conduct the analysis, we associate the energy in the long-wavelength range $\lambda_z \geq 0.5\lambda$ with the vortex mode. This threshold is demonstrated with vertical lines in figure 23. Figure 24 shows the fraction of the streamwise turbulent kinetic energy in the range $\lambda_z \geq 0.5\lambda$, i.e. $\mathcal{Y}_{xx}(0.5\lambda)$, evaluated along $\mathbf{x}_P(\theta)$ and $\mathbf{x}_S(\theta)$. We see that the $P^+ - S^-$ dipole is unstable to the vortex mode, whose energy grows during the motion of the dipole towards the crest. When the vortices pass the crest at $x/\eta = 6$, coherent motions related to the vortex mode contain a significant portion of the total streamwise fluctuation energy – approximately 70% in the P -vortex core, and approximately 75% in the S -vortex core. Large-scale dynamics of vortices differs following their ejection from the crest. We have previously seen that S^- vortex loses most of the

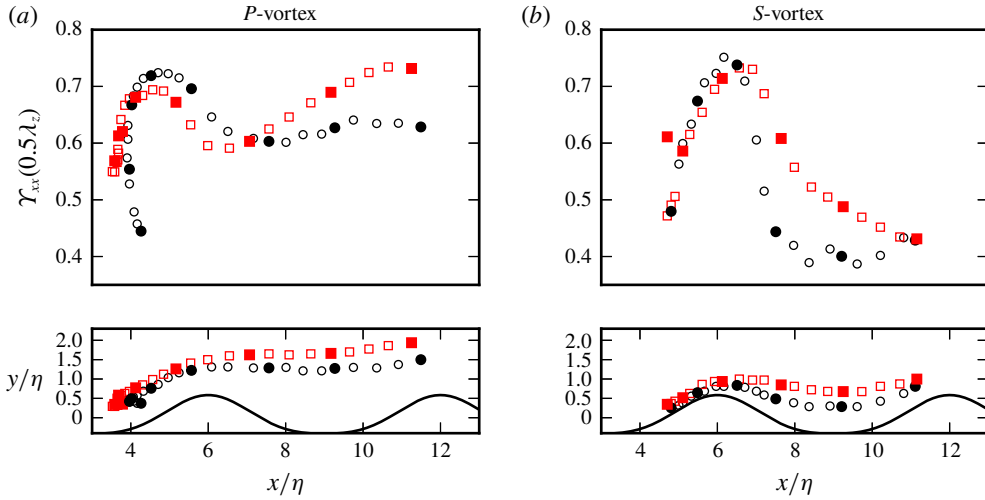


FIGURE 24. (Colour online) The cumulative fraction of the streamwise turbulent kinetic energy in transverse wavelengths $\lambda_z \geq 0.5\lambda$, cf. (6.5). (a) Evaluated on $\mathbf{x}_P(\theta)$ in $4\pi/32 \leq \theta \leq \pi$; (b) evaluated on $\mathbf{x}_S(\theta)$ in $12\pi/32 \leq \theta \leq \pi$, cf. table 5 for trajectories $\mathbf{x}_P(\theta)$ and $\mathbf{x}_S(\theta)$. (○) Case C1; (□) Case C2. Each data point is separated by $\pi/32$ in time, and filled markers indicate every fourth data point.

large-scale energy after it passes the crest. This is also clearly seen in figure 24(b), where $\Upsilon_{xt}(0.5\lambda)$ decreases rapidly to approximately 40% following $x/\eta > 6.5$. In contrast, the coherent large-scale motions remain active in the primary vortex, and their fractional contributions to the overall energy remain above 60%. This difference between *P*- and *S*-vortices is likely due to their respective distances to the ripple surface, which seems to dissolve the portion of the vortex mode passing nearby.

Figure 23 showed that preferred spanwise spacings of the three-dimensional structures driven by the energetic vortex mode vary in the range $0.6 < \lambda_z/\lambda < 0.9$. These values are in the same range with the spanwise spacing of the brick patterns ($0.6 < \lambda_z/\lambda < 1.3$) observed by Ourmières & Chaplin (2004) in disturbed-laminar regimes over vortex ripples. Moreover, we have observed in § 6.1 that the arrangement of large-scale structures in Case C1 is also reminiscent of brick patterns. In this regard, the current study provides preliminary evidence for the emergence of these subharmonic flow patterns in fully turbulent regimes.

Canals & Pawlak (2011) also reported dominant large-scale structures on a vortex dipole, which is formed around a single ripple attached to an oscillating tray. These structures were formed by an elliptic instability of the strained vortex cores, and had spanwise spacings in the range $2 < \lambda_z/r < 5$, where r is the vortex-core radius. If we assume the radius of the vortex cores in our study is approximately $r \approx \eta$, then there is a good overlap between the observed spanwise spacings in our simulations ($3.6 < \lambda_z/\eta < 5.4$) and in experiments by Canals & Pawlak (2011). Furthermore, we have seen in figure 24 that the vortex mode energy increases during the motion of the dipole towards the crest in the range $8\pi/32 \leq \theta \leq 16\pi/32$. This is the stage where the vortices mutually strain each other to elliptic forms (cf. figures 4c–e and 5c–e in § 3). Therefore, we believe that the observed vortex mode is driven by elliptic instabilities of coherent-vortex cores.

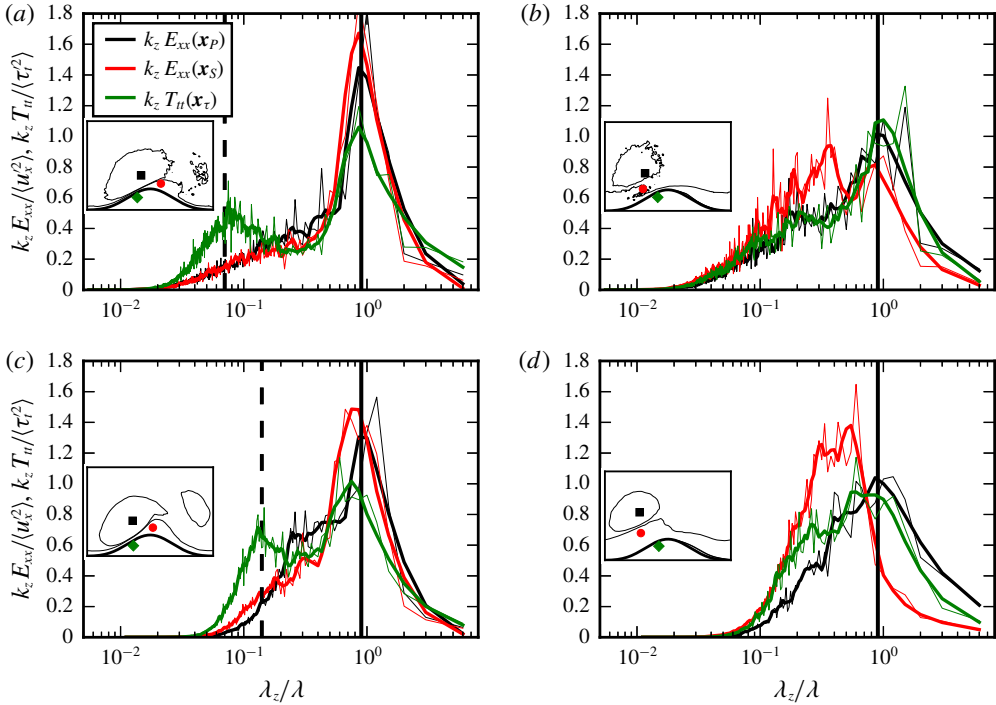


FIGURE 25. (Colour online) Premultiplied streamwise turbulent kinetic energy spectra evaluated at the P -vortex core (black) and at the S -vortex core (red), and premultiplied wall-shear-stress spectra evaluated at the local wall-shear-stress maximum (green). (a,c) $\theta = 20\pi/32$; (b,d) $\theta = 31\pi/32$. (a,b) Case C1; (c,d) Case C2. The thin lines show raw spectra without the Savitzky–Golay filter. The spectra are normalized with the local average values such that areas under the curves are equal to unity. The markers in insets show the respective probing points \mathbf{x}_P , \mathbf{x}_S and \mathbf{x}_τ , where the same colour coding with the lines is employed.

We have shown in § 6.1 that large-scale momentum structures have strong footprints on the wall. Figure 25 elaborates this by comparing the premultiplied spanwise spectra evaluated at the cores of primary and secondary vortices, $\kappa_z E_{xx}(\mathbf{x}_P)$, $\kappa_z E_{xx}(\mathbf{x}_S)$ and at the local wall-shear-stress peak, $\kappa_z T_H(\mathbf{x}_\tau)$, for the phases previously employed in figure 21, i.e. $\theta = 20\pi/32$, $31\pi/32$. All spectra are normalized with local fluctuation levels such that the areas under the curves are equal to unity. It is observed in both cases at $\theta = 20\pi/32$ that the vortex mode yields a dominant peak at $\lambda_z = 0.9\lambda$ in all three spectra, cf. solid vertical lines in figure 25(a,c). There is a second peak with shorter wavelength in the wall-shear-stress spectra, cf. dashed vertical lines in figure 25(a,c). This peak appears to be Reynolds number dependent, and occurs on smaller wavelengths in Case C1. The secondary peak is not observed in the vortex cores, as it is related to the streaky velocity field induced by streamwise vortices near the wall. At $\theta = 31\pi/32$, the second peak appears to be absent in $\kappa_z T_H(\mathbf{x}_\tau)$, cf. figure 25(b,d). The vortex mode, now active only in the P^+ vortex, still influences the wall-shear-stress spectrum at this phase, cf. solid lines at $\lambda_z = 0.9\lambda$ in figure 25(b,d). The mode is less dominant at this phase, and the peaks are less pronounced. Moreover, $\kappa_z E_{xx}(\mathbf{x}_S)$ does not contain such a peak, as S^- vortex has

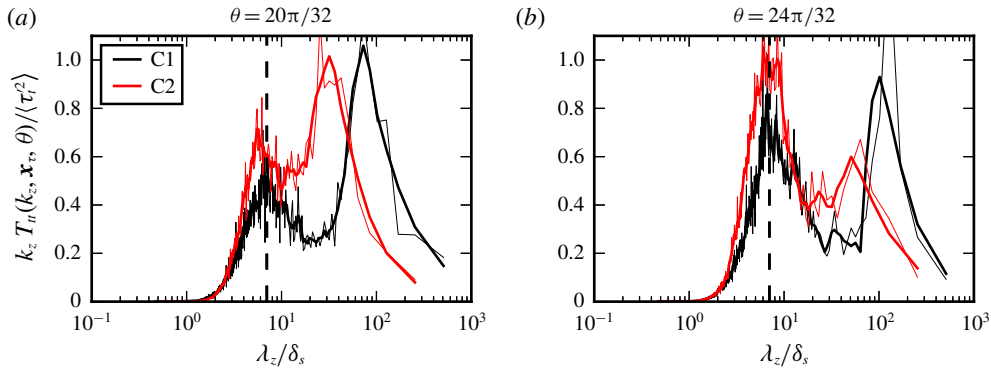


FIGURE 26. (Colour online) Premultiplied spectra of tangential wall-shear-stress fluctuations presented as functions of spanwise wavelength scaled with the Stokes length ($\delta_s = \sqrt{2\nu/\omega}$). The spectra are evaluated at $\mathbf{x}_\tau(20\pi/32)$ in (a) and at $\mathbf{x}_\tau(24\pi/32)$ in (b). The dashed lines show $\lambda_z/\delta_s = 7$. The thin lines represent the raw spectra.

transitioned to a less coherent state after leaving the crest, as previously shown in figures 23(b,d) and 24(b).

We now turn to the scaling of organized streamwise vortices. A natural length scale to relate the spacing of streamwise vortices is the boundary-layer thickness over the vortex ripple, which is expected to be related to the Stokes length $\delta_s = \sqrt{2\nu/\omega}$. Figure 26 shows premultiplied wall-shear-stress spectra at $\theta = 20\pi/32$, $24\pi/32$ as functions of wavelengths that are normalized with the Stokes length. We see that the streamwise structures scale well with the Stokes length for the two cases, i.e. the short-wavelength peaks collapse well at $\lambda_z/\delta_s \approx 7$. The same value ($7\delta_s$) is also reported in Blondeaux *et al.* (2004) for the spanwise spacing of streamwise vortices forming along the upstream side of ripples (cf. figure 9 and its discussion on p. 224 in Blondeaux *et al.* (2004)). Although our limited dataset prevents a further elaboration of this result, it is informative to compare this spacing with the one produced by centrifugal instabilities over vortex ripples, as curved ripple walls can promote these instabilities. Using a wide variety of configurations, Ourmieres & Chaplin (2004) analysed these features in disturbed-laminar regimes. They showed that centrifugal instabilities produce spanwise patterns along the vortex columns with a well-defined spacing of $\lambda_z/\delta_s \approx \sqrt{2}\lambda^2/A\eta$. In this regard, the spacing of the streamwise structures in our DNS experiments is in the same range but slightly smaller, i.e. $\lambda_z/\delta_s \approx 7 \approx \lambda^2/A\eta$. These results point towards possible relations between the short spanwise wavelength patterns in disturbed-laminar and turbulent conditions. Exploring these links further may be an interesting future study that can shed light on the origin and scaling of the streamwise structures over vortex ripples.

7. Conclusions

We have conducted a DNS study to investigate the sinusoidal oscillatory flow over a two-dimensional wavy bottom. The model conditions were selected to mimic wave-driven flow conditions above long crested sand ripples in coastal regions. Two different Reynolds numbers were involved. The higher-*Re* case was found to produce a fully developed turbulent flow in which energy-containing and dissipative motions concentrate at exclusive scales.

The oscillatory flow is dominated by coherent columnar vortices of two types. A primary lee vortex is formed during the deceleration phase by the separation of the boundary layer at the ripple crest. When this vortex becomes stronger, the gradients in its pressure field give rise to a secondary flow separation, and eventually a secondary vortex forms at the lee of the ripple. With further weakening of the free-stream velocity, the primary and secondary vortices form a counter-rotating vortex dipole, and move towards the crest. They eventually eject themselves over the ripple crest with their mutually induced velocities. At this moment, they create a high-speed jet near the crest with peak velocities reaching twice that of the maximum free-stream velocity. The inclination angle of the ejection showed a Reynolds number dependence. As the boundary layers are thinner in the higher- Re case, the secondary separation and succeeding vortex creation are bound to a smaller volume beneath the primary vortex. Consequently, the primary vortex is less repelled away from the ripple, and the resulting ejection angle is more horizontal. This paves the way for more intense wall–vortex interactions in the higher- Re case.

Coherent vortices are the main transport means for turbulent kinetic energy and enstrophy. The boundary layers on the ripple surface are only mildly turbulent in both cases. The main production zones are the free separated layers with intense shear, and the main dissipation regions are the vortex cores and boundary layers. The global turbulence production rate peaks twice over a half-cycle. The first peak occurs close to the start of the deceleration phase, and the second one takes place when the vortices eject themselves over the ripple. This initial peak is weak in the lower- Re case, as milder wall–vortex interactions in this case leave quieter flow in the lee of the ripples for the subsequent vortex-formation stage. The turbulent dissipation is most intense during the formation of coherent vortices.

The structural characteristics of coherent vortices are investigated by evaluating their statistics along their path and by visualizing their instantaneous regions with high enstrophy. In the beginning of their lives, coherent vortices keep their spanwise coherence, and are in the form of turbulent vortex clouds that fill the entire spanwise extent of the computational domain. A large-scale vortex mode with transverse wavelengths in the range $0.6 < \lambda_z/\lambda < 0.9$ develops along the vortex column when the vortex dipole moves towards the ripple crest in the ejection process. At this phase, the vortex cores are strained by mutual induction, and vortices become more elliptic. Therefore, this vortex mode is possibly a result of an elliptic instability occurring on the vortex dipole, which was previously observed by Canals & Pawlak (2011) in different oscillatory flow settings. Following their detachment from the ripple, the vortices in the higher- Re case begin to lose their spanwise coherence due to the large-scale vortex mode, and develop an external intermittency along the transverse direction. Consequently, they break down into turbulent vortex clusters whose streamwise arrangement is reminiscent of a brick pattern. The breakdown of spanwise coherence and resulting subharmonic vortex patterns are not observed in the lower- Re case.

Furthermore, we have observed secondary structures near to the wall in the form of elongated streamwise vortices, which become more evident during the vortex-ejection stage. These highly anisotropic structures have shorter spanwise spacing. The spectral peaks related to these structures are observed to collapse well at $\lambda_z/\delta_s \approx 7$ when scaled with the Stokes length.

Coherent spanwise vortices have been found to have strong footprints in the near-wall region. During their formation, the primary vortex induces a wall shear in a reverse direction to the free-stream velocity. This wall shear becomes more

pronounced when the primary and secondary vortices accelerate towards the crest, and produce the high-speed wall jet. This is the phase when the highest values in the local phase-averaged wall shear stress are observed. Moreover, the coherent vortices also yield strong spanwise inhomogeneity in the wall shear stress as they evolve. In the ejection stage, both large-scale structures driven by the vortex mode and streamwise-vortex structures impose strong fluctuations on the ripple surface. This creates a bimodal premultiplied energy spectrum with two distinctive peaks for wall-shear-stress fluctuations. When decaying coherent vortices arrive at the neighbouring ripple towards the end of the free-stream acceleration, their wall-attached portions sweep the ripple surface and dramatically increase the wall shear stress in their convection direction. This leads to highly skewed probability density functions with long tails for the local wall shear stresses in the contact areas.

The findings in this study provide important implications for the breakdown of long crested sand ripples into three-dimensional forms. Large-scale three-dimensional patterns along the transverse vortex columns could produce inhomogeneous sediment suspension and deposition processes. Furthermore, spanwise variations in the wall shear stress can possibly lead inhomogeneous near-surface sediment motions. In this regard, further knowledge about the origin and scaling behaviour of the observed three-dimensional instabilities can be of key practical importance. Experimentation in a wider parameter space is necessary to gain these insights.

Acknowledgements

The authors gratefully acknowledge financial support from the Tier-1 research project funded by the Ministry of Education of Singapore (WBS:R-302-000-126-112). The computational work for this article was fully performed on resources of the National Supercomputing Centre, Singapore (<https://www.nsc.sg>).

Appendix A. Spectral assessment of the spatial resolution

In this appendix, we further assess the resolution of the dissipative motions using one-dimensional spectra in the homogenous spanwise direction. This spectral analysis tests the spanwise resolution. As dissipative motions are essentially isotropic, and the largest grid spacings in Kolmogorov units have similar values in the x - y plane and the in z direction (compare the largest values in figure 3*d,e* in § 2.3), the results are also instructive for the spatial resolution in the x - y plane.

We start with proving the spectra for Kolmogorov's laws (Kolmogorov 1941), assuming they are applicable in the energetic locations of our flows. We have seen in § 5 that turbulent kinetic energy concentrates in the core of coherent vortices P and S , on which the trajectories \mathbf{x}_P and \mathbf{x}_S are defined. Figure 27 shows the spanwise energy spectra of streamwise velocity fluctuations evaluated at \mathbf{x}_P and \mathbf{x}_S at several representative phases with high turbulent kinetic energy. The spectra are presented in Kolmogorov units, i.e. λ_z/l_η , and are normalized by $(\varepsilon\nu^5)^{1/4}$ such that all lines should collapse on the universal Kolmogorov spectrum in the highest wavenumbers, i.e. in the dissipative range. Pope (2000) presented such a collapse for $\kappa_x l_\eta > 0.1$ using the streamwise spectra of many different types of turbulent flows. We see in figure 27(*a,b*) that all spectra lie on a single curve for $\kappa_z l_\eta > 0.1$ also in our simulations, which shows that dissipative motions are well resolved. In the inertial range, the Kolmogorov spectrum follows the $-5/3$ power law (Pope 2000)

$$\frac{E_{xx}(\kappa_z)}{(\varepsilon\nu^5)^{1/4}} = \frac{4}{3} C_k (\kappa_z l_\eta)^{-5/3}, \quad (\text{A } 1)$$

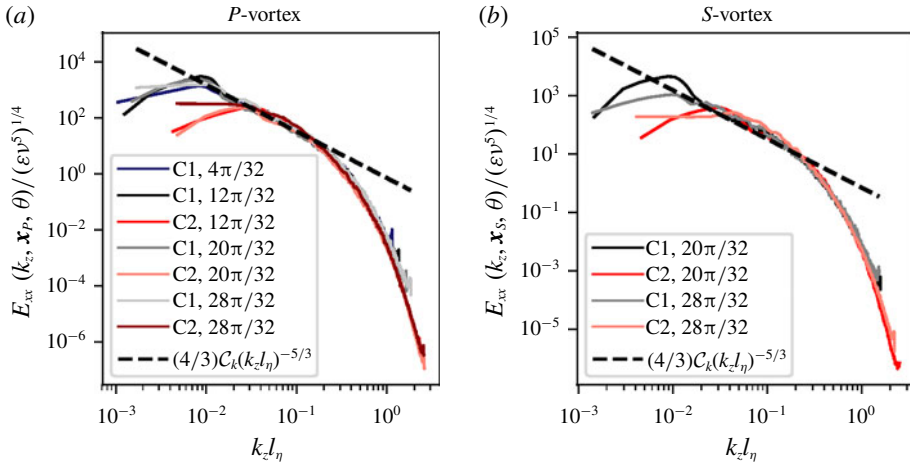


FIGURE 27. (Colour online) Spanwise energy spectra of streamwise-velocity fluctuations evaluated at the coherent-vortex cores \mathbf{x}_p and \mathbf{x}_s and presented as functions of the spanwise wavenumber κ_z in local Kolmogorov units ($l_\eta = (v^3/\epsilon)^{1/4}$).

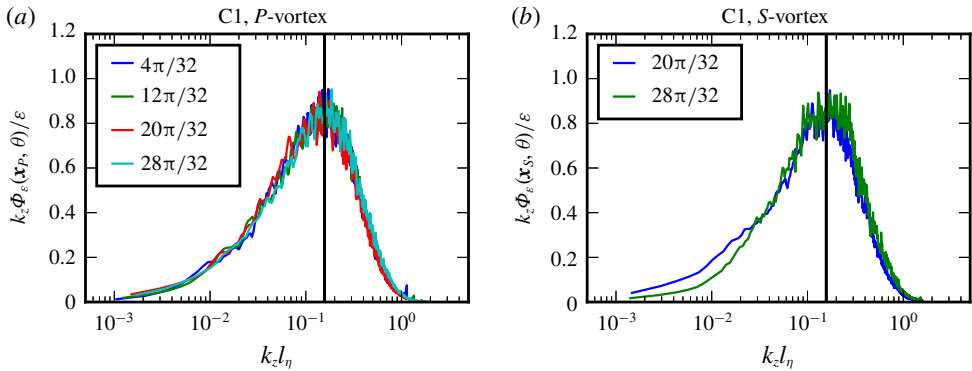


FIGURE 28. (Colour online) One-dimensional premultiplied enstrophy spectra evaluated at the coherent-vortex cores \mathbf{x}_p and \mathbf{x}_s and presented as functions of the spanwise wavenumber κ_z in local Kolmogorov units ($l_\eta = (v^3/\epsilon)^{1/4}$). The vertical lines show $\kappa_z l_\eta = 2\pi/40$.

where $C_k = 0.53$ is the universal Kolmogorov constant (Sreenivasan 1995), and the factor $4/3$ is added for using the transverse velocity spectra. The dashed lines in figure 27(a,b) represents the power law. We see that $-5/3$ power law is applicable at the coherent-vortex cores of both cases, and the spectra follows the dashed line in the inertial range starting from $\kappa_z l_\eta < 0.1$. The inertial range extends to lower wavenumbers in C1 due to higher Reynolds number in this case.

Figure 28 shows the premultiplied enstrophy spectra evaluated at the coherent-vortex cores at the same phases with figure 27. For brevity, only results for C1 are presented. We see that vorticity concentrates around $\kappa_z l_\eta \approx 2\pi/40$, and all curves collapse in the dissipation range, i.e. $\kappa_z l_\eta > 0.1$. The peak at $\kappa_z l_\eta \approx 2\pi/40$ appears to be universal for small-scale quantities such as vorticity or strain rate at sufficiently high Reynolds numbers, e.g. Jiménez (2013) also showed a peaking of the dissipation spectra around

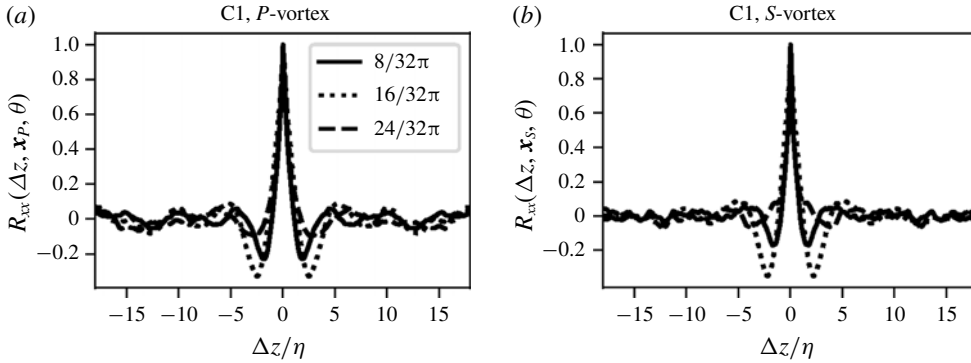


FIGURE 29. Spanwise autocorrelations of streamwise velocity evaluated at the coherent-vortex cores \mathbf{x}_p and \mathbf{x}_s in Case C1.

$\kappa_z l_\eta \approx 2\pi/40$ in the logarithmic layer of a wall-bounded flow. Figure 28 also shows that smallest scales of the flow are well resolved in our DNS experiments. There are no noticeable aliasing errors due to underresolution in S -vortex cores, cf. figure 28(b). We observe only a minor artificial rise due to aliasing in highest wavenumbers at $(\mathbf{x}_p(4\pi/32), 4\pi/32)$, cf. the blue line in $\kappa_z l_\eta \geq 1$ in figure 28(a). In their DNS study of channel flow, Del Álamo *et al.* (2006) calculated the percentage of enstrophy residing in the aliased wavenumber range and found values in the range 2–3%. We did a similar calculation for the spectra at $(\mathbf{x}_p(4\pi/32), 4\pi/32)$ and found that the enstrophy residing in the aliased range ($\kappa_z l_\eta \geq 1$) is less than 0.2% of the total enstrophy $\mathcal{E}(\mathbf{x}_p(4\pi/32), 4\pi/32)$.

Appendix B. Analysis of the computational domain size

In this section, we assess the computational domain lengths in the spanwise and vertical directions. In order to validate the spanwise extent of the domain, the two-point correlation function in the spanwise direction, i.e.

$$\mathcal{R}_{ij}(\Delta z, x, y, \theta) = \frac{\langle u'_i(x, y, z, \theta)u'_j(x, y, z + \Delta z, \theta) \rangle}{\langle u'_i(x, y, z + \Delta z, \theta)^2 \rangle^{1/2} \langle u'_i(x, y, z, \theta)^2 \rangle^{1/2}}, \tag{B 1}$$

is employed. Figure 29 shows the spanwise correlations of streamwise velocity fluctuations at the coherent-vortex cores of Case C1 (similar results are applicable to C2). Mahesh & Moin (1998) suggests two-point correlation functions should decay completely within the half of the length of the domain, in order to prevent the interference of periodic boundaries with the largest scales of the flow. We see in figures that the spanwise domain length satisfies this condition. The correlation function decays to negligible values for $|\Delta z| > 6\eta (= \lambda)$ with somewhat more noise beyond $|\Delta z| > 6\eta$ in the case of P -vortex, cf. figure 29(a).

We now turn to the verification of the extent of the vertical domain. For this purpose, we investigate horizontally averaged fields, which are defined as

$$\tilde{\langle \mathbf{u} \rangle}(y, \theta) = \frac{1}{\lambda} \int_0^\lambda \langle \mathbf{u} \rangle(x, y, \theta) dx. \tag{B 2}$$

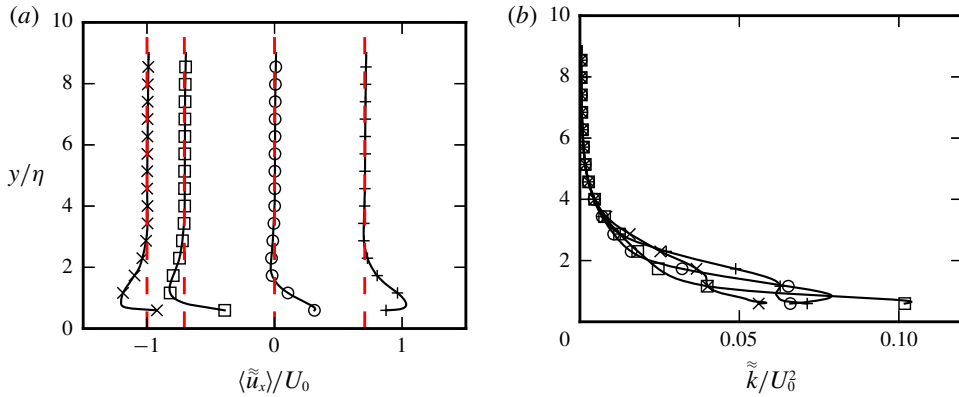


FIGURE 30. (Colour online) Horizontally averaged streamwise velocity (a) and turbulent kinetic energy (b). $(-\times)$: $\theta = 0$; $(-\square)$: $\theta = 8\pi/32$; $(-\circ)$: $\theta = 16\pi/32$; $(-+)$: $\theta = 24\pi/32$. Dashed lines in (a) show the value of the free-stream velocity ($u_0(\theta)$) at respective phases.

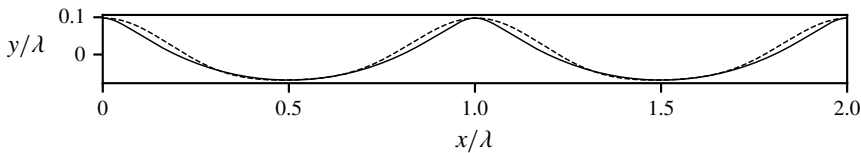


FIGURE 31. Comparison of the ripple profiles considered in this work (dashed line) and in du Toit & Sleath (1981) (solid line).

Figure 30 shows the horizontally averaged streamwise velocity and TKE at several phases in the half-cycle of Case C1. In the free-stream, streamwise velocity should return to irrotational velocity u_0 (cf. (2.4)) and TKE should vanish. We see in figures that these conditions are satisfied for $y > 6\eta$. Therefore, we conclude that the vertical extent of our computational domain is sufficiently large to allow free-stream conditions away from the bottom.

Appendix C. Comparisons to experimental data

Although there are quite a few experimental studies on oscillatory flow over rippled beds, an equivalent experiment to Cases C1 and C2 has not yet been conducted. Laboratory flows are usually at higher Reynolds numbers than attained in this work and K_C number and ripple geometries also vary. Despite this limitation, we can examine some common flow features using experimental data with similar configurations. To this end, we consider an experiment by du Toit & Sleath (1981) (TS81 henceforth), which was conducted in an oscillating water tunnel using self-formed ripples. The flow parameters in this experiment are $Re = 21\,617$ and $K_C = 4.46$. The ripple steepness is the same as our cases ($s \approx 0.17$), and the ripple profile is shown by the solid line in figure 31. This profile is slightly sharper towards the crest than the one considered in this work (given by the dashed line in figure 31). Only Case C1 will be considered in the comparison, as it has a closer Reynolds number to the selected experiment.

Figure 32 shows the intra-period variations of phase-averaged streamwise velocity and streamwise turbulent intensity at two selected points. The experimental data are

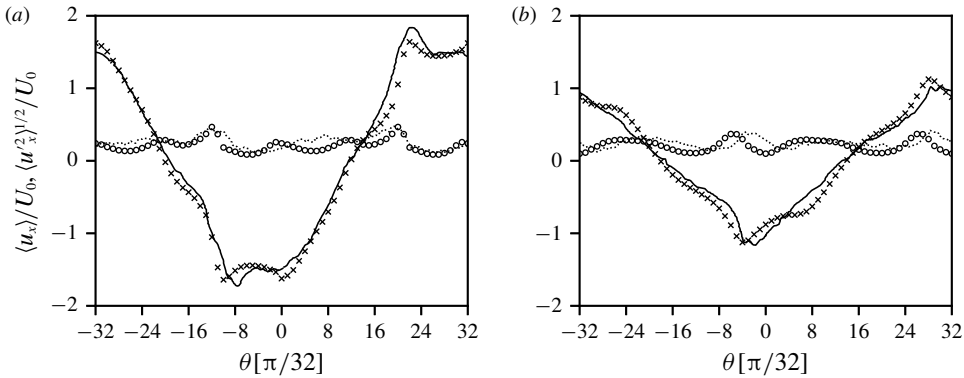


FIGURE 32. Intra-period variations of phase-averaged streamwise velocity and turbulent intensity over the crest at $(x_c, (y - y_c)/\delta_s = 1.44)$ (a) and over the trough at $(x_t, (y - y_c)/\eta = 0.058)$ (b), where subscripts c and t refer to the coordinates of the crest and trough, respectively. (×): $\langle u_x \rangle / U_0$, Case C1; (—): $\langle u_x \rangle / U_0$ digitized from figure 15 in du Toit & Sleath (1981); (○): $\langle u_x^2 \rangle^{1/2} / U_0$, Case C1; (⋯): $\langle u_x^2 \rangle^{1/2} / U_0$ digitized from figure 18 in du Toit & Sleath (1981).

digitized from figures 15 and 18 in TS81. The first probing point is slightly above the ripple crest at $(x_c, (y - y_c)/\delta_s = 1.44)$ and the second point is located above the ripple trough close to crest level at $(x_t, (y - y_c)/\eta = 0.058)$, where subscripts c and t refer to the coordinates of the ripple crest and the ripple trough. The variations in the respective half-cycles of the experimental data are not the mirror image of each other due to some experimental errors.

We see in figure 32(a) that the mean streamwise velocity over the ripple crest agrees well with the experimental data within the margin of experimental errors. The peaks in velocity occur when the coherent vortices are washed over the crest at $\theta \approx -8/32, 24/32\pi$ and when the free-stream velocity has maximum magnitude at $\theta = 0, \pi$. Turbulent intensity peaks during the vortex ejection at $\theta \approx -8/32, 24/32\pi$, and the magnitude and phase of this peak match well. The turbulent intensity between $-\pi \leq \theta \leq -24/32\pi$ ($0 \leq \theta \leq 8/32\pi$) is higher in TS81.

Figure 32(b) shows the variations at the point located over the ripple trough. It is observed that the maximum amplitude of the streamwise velocity is approximately U_0 at this location for both Case C1 and TS81. This peak in the velocity occurs when the coherent vortices pass over the ripple trough. This event takes place at $\theta \approx -4/32, 28/32\pi$ in C1 – approximately $\theta \approx 2/32$ earlier than TS81. A similar delay applies to turbulence intensities, which peak also during the passage of the vortex. This minor phase difference is likely related to the difference in K_C number, which is slightly lower in TS81 ($K_C = 4.46$) than C1 ($K_C = 5.24$), hence the vortex passage corresponds to a later phase.

REFERENCES

BAGNOLD, R. A. & TAYLOR, G. 1946 Motion of waves in shallow water. Interaction between waves and sand bottoms. *Proc. R. Soc. Lond. A* **187** (1008), 1–18.
 BATCHELOR, G. K. 2000 *An Introduction to Fluid Dynamics*. Cambridge University Press.
 BATCHELOR, G. K. & TOWNSEND, A. A. 1949 The nature of turbulent motion at large wave-numbers. *Proc. R. Soc. Lond. A* **199** (1057), 238–255.

- BLONDEAUX, P., SCANDURA, P. & VITTORI, G. 2004 Coherent structures in an oscillatory separated flow: numerical experiments. *J. Fluid Mech.* **518**, 215–229.
- BLONDEAUX, P. & VITTORI, G. 1991 Vorticity dynamics in an oscillatory flow over a rippled bed. *J. Fluid Mech.* **226**, 257–289.
- BLONDEAUX, P. & VITTORI, G. 1999 Boundary layer and sediment dynamics under sea waves. *Adv. Coastal Ocean Engng* **4**, 133–190.
- BOYD, J. P. 2001 *Chebyshev and Fourier Spectral Methods*. Courier Corporation.
- BUXTON, O. R. H., BREDI, M. & CHEN, X. 2017 Invariants of the velocity-gradient tensor in a spatially developing inhomogeneous turbulent flow. *J. Fluid Mech.* **817**, 1–20.
- CANALS, M. & PAWLAK, G. 2011 Three-dimensional vortex dynamics in oscillatory flow separation. *J. Fluid Mech.* **674**, 408–432.
- CANTWELL, C. D. *et al.* 2015 Nektar++: an open-source spectral/hp element framework. *Comput. Phys. Commun.* **192**, 205–219.
- CORRSIN, S. 1958 Local isotropy in turbulent shear flow. *Tech. Rep.* NACA-RM-58B11. National Advisory Committee for Aeronautics.
- DARWIN, G. H. 1883 On the formation of ripple-mark in sand. *Proc. R. Soc. Lond. A* **36** (228–231), 18–43.
- DEL ÁLAMO, J. C., JIMENEZ, J., ZANDONADE, P. & MOSER, R. D. 2006 Self-similar vortex clusters in the turbulent logarithmic region. *J. Fluid Mech.* **561**, 329–358.
- DIMOTAKIS, P. E. 2000 The mixing transition in turbulent flows. *J. Fluid Mech.* **409** (1), 69–98.
- DOLIGALSKI, T. L., SMITH, C. R. & WALKER, J. D. A. 1994 Vortex interactions with walls. *Annu. Rev. Fluid Mech.* **26** (1), 573–616.
- EARNSHAW, H. C. & GREATHEAD, C. A. 1998 Dynamics of ripple bed vortices. *Exp. Fluids* **25** (3), 265–275.
- FREDSØE, J., ANDERSEN, K. H. & SUMER, B. M. 1999 Wave plus current over a ripple-covered bed. *Coast. Engng* **38** (4), 177–221.
- GHODKE, C. D. & APTE, S. V. 2016 DNS study of particle-bed–turbulence interactions in an oscillatory wall-bounded flow. *J. Fluid Mech.* **792**, 232–251.
- GOMES-FERNANDES, R., GANAPATHISUBRAMANI, B. & VASSILICOS, J. C. 2014 Evolution of the velocity-gradient tensor in a spatially developing turbulent flow. *J. Fluid Mech.* **756**, 252–292.
- GRIGORIADIS, D. G. E., DIMAS, A. A. & BALARAS, E. 2012 Large-eddy simulation of wave turbulent boundary layer over rippled bed. *Coast. Engng* **60**, 174–189.
- GSCHWIND, P., REGELE, A. & KOTTKE, V. 1995 Sinusoidal wavy channels with Taylor–Goertler vortices. *Exp. Therm. Fluid Sci.* **11** (3), 270–275.
- GUALA, M., HOMMEMA, S. E. & ADRIAN, R. J. 2006 Large-scale and very-large-scale motions in turbulent pipe flow. *J. Fluid Mech.* **554**, 521–542.
- GÜNTHER, A. & VON ROHR, P. R. 2003 Large-scale structures in a developed flow over a wavy wall. *J. Fluid Mech.* **478**, 257–285.
- HARA, T. & MEI, C. C. 1990 Centrifugal instability of an oscillatory flow over periodic ripples. *J. Fluid Mech.* **217**, 1–32.
- HARE, J., HAY, A. E., ZEDEL, L. & CHEEL, R. 2014 Observations of the space-time structure of flow, turbulence, and stress over orbital-scale ripples. *J. Geophys. Res.* **119** (3), 1876–1898.
- HONJI, H., KANEKO, A. & MATSUNAGA, N. 1980 Flows above oscillatory ripples. *Sedimentology* **27** (2), 225–229.
- HOYAS, S. & JIMÉNEZ, J. 2006 Scaling of the velocity fluctuations in turbulent channels up to $Re_\tau = 2003$. *Phys. Fluids* **18** (1), 011702.
- HUSSAIN, A. K. M. F. 1986 Coherent structures and turbulence. *J. Fluid Mech.* **173**, 303–356.
- HUTCHINS, N. & MARUSIC, I. 2007 Evidence of very long meandering features in the logarithmic region of turbulent boundary layers. *J. Fluid Mech.* **579**, 1–28.
- JENSEN, B. L., SUMER, B. M. & FREDSOE, J. 1989 Turbulent oscillatory boundary layers at high Reynolds numbers. *J. Fluid Mech.* **206**, 265–297.
- JESPERSEN, T. S., THOMASSEN, J. Q., ANDERSEN, A. & BOHR, T. 2004 Vortex dynamics around a solid ripple in an oscillatory flow. *Eur. Phys. J. B* **38** (1), 127–138.
- JIMÉNEZ, J. 2012 Cascades in wall-bounded turbulence. *Annu. Rev. Fluid Mech.* **44**, 27–45.

- JIMÉNEZ, J. 2013 Near-wall turbulence. *Phys. Fluids* **25** (10), 101302.
- JORDAN, P. & COLONIUS, T. 2013 Wave packets and turbulent jet noise. *Annu. Rev. Fluid Mech.* **45**, 173–195.
- KARNIADAKIS, G. E. 1990 Spectral element-Fourier methods for incompressible turbulent flows. *Comput. Meth. Appl. Mech. Engng* **80** (1), 367–380.
- KARNIADAKIS, G. E., ISRAELI, M. & ORSZAG, S. A. 1991 High-order splitting methods for the incompressible Navier–Stokes equations. *J. Comput. Phys.* **97** (2), 414–443.
- KARNIADAKIS, G. E. & SHERWIN, S. J. 2005 *Spectral/hp Methods for Computational Fluid Dynamics*. Oxford University Press.
- KOLMOGOROV, A. 1941 The local structure of turbulence in incompressible viscous fluid for very large Reynolds numbers. *Dokl. Akad. Nauk SSSR* **30**, 301–305.
- LEE, M. J., KIM, J. & MOIN, P. 1990 Structure of turbulence at high shear rate. *J. Fluid Mech.* **216**, 561–583.
- LONGUET-HIGGINS, M. S. 1981 Oscillating flow over steep sand ripples. *J. Fluid Mech.* **107**, 1–35.
- LOZANO-DURÁN, A. & JIMÉNEZ, J. 2014 Time-resolved evolution of coherent structures in turbulent channels: characterization of eddies and cascades. *J. Fluid Mech.* **759**, 432–471.
- LUMLEY, J. L. 1979 Computational modeling of turbulent flows. *Adv. Appl. Mech.* **18**, 123–176.
- MAHESH, K. & MOIN, P. 1998 Direct numerical simulation: a tool in turbulence research. *Annu. Rev. Fluid Mech.* **30** (1), 539–578.
- MAZZUOLI, M. & VITTORI, G. 2016 Transition to turbulence in an oscillatory flow over a rough wall. *J. Fluid Mech.* **792**, 67–97.
- MAZZUOLI, M., VITTORI, G. & BLONDEAUX, P. 2011 Turbulent spots in oscillatory boundary layers. *J. Fluid Mech.* **685**, 365–376.
- MEI, C. C. & LIU, P. L. 1993 Surface waves and coastal dynamics. *Annu. Rev. Fluid Mech.* **25** (1), 215–240.
- NAKATO, T., KENNEDY, J. F., GLOVER, J. R. & LOCHER, F. A. 1977 Wave entrainment of sediment from rippled beds. *J. Waterways Port Coast. Ocean Div. ASCE* **103** (1), 83–99.
- NEU, J. C. 1984 The dynamics of stretched vortices. *J. Fluid Mech.* **143**, 253–276.
- NICHOLS, C. S. & FOSTER, D. L. 2007 Full-scale observations of wave-induced vortex generation over a rippled bed. *J. Geophys. Res.* **112**, C10015.
- NIELSEN, P. 1992 *Coastal Bottom Boundary Layers and Sediment Transport*. World Scientific Publishing.
- O'DONOGHUE, T., DOUCETTE, J. S., VAN DER WERF, J. J. & RIBBERINK, J. S. 2006 The dimensions of sand ripples in full-scale oscillatory flows. *Coast. Engng* **53** (12), 997–1012.
- OKUBO, A. 1970 Horizontal dispersion of floatable particles in the vicinity of velocity singularities such as convergences. *Deep Sea Res. Ocean Abstracts* **17** (3), 445–454.
- OURMIERES, Y. & CHAPLIN, J. R. 2004 Visualizations of the disturbed-laminar wave-induced flow above a rippled bed. *Exp. Fluids* **36** (6), 908–918.
- OZDEMIR, C. E., HSU, T.-J. & BALACHANDAR, S. 2014 Direct numerical simulations of transition and turbulence in smooth-walled Stokes boundary layer. *Phys. Fluids* **26** (4), 045108.
- POPE, S. B. 2000 *Turbulent Flows*. Cambridge University Press.
- ROBINSON, S. K. 1991 Coherent motions in the turbulent boundary layer. *Annu. Rev. Fluid Mech.* **23** (1), 601–639.
- ROUSON, D. W. & EATON, J. K. 2001 On the preferential concentration of solid particles in turbulent channel flow. *J. Fluid Mech.* **428**, 149–169.
- SAFFMAN, P. G. 1978 Problems and progress in the theory of turbulence. In *Structure and Mechanisms of Turbulence II*, pp. 273–306. Springer.
- SALON, S., ARMENIO, V. & CRISE, A. 2007 A numerical investigation of the Stokes boundary layer in the turbulent regime. *J. Fluid Mech.* **570**, 253–296.
- SARIC, W. S. 1994 Görtler vortices. *Annu. Rev. Fluid Mech.* **26** (1), 379–409.
- SATO, S., MIMURA, N. & WATANABE, A. 1985 Oscillatory boundary layer flow over rippled beds. In *Proceedings of the 19th International Conference on Coastal Engineering*, pp. 2293–2309. American Society of Civil Engineers.

- SAVITZKY, A. & GOLAY, M. J. E. 1964 Smoothing and differentiation of data by simplified least squares procedures. *Analyt. Chem.* **36** (8), 1627–1639.
- SCANDURA, P., FARACI, C. & FOTI, E. 2016 A numerical investigation of acceleration-skewed oscillatory flows. *J. Fluid Mech.* **808**, 576–613.
- SCANDURA, P., VITTORI, G. & BLONDEAUX, P. 2000 Three-dimensional oscillatory flow over steep ripples. *J. Fluid Mech.* **412**, 355–378.
- DA SILVA, C. B., HUNT, J. C. R., EAMES, I. & WESTERWEEL, J. 2014 Interfacial layers between regions of different turbulence intensity. *Annu. Rev. Fluid Mech.* **46**, 567–590.
- SREENIVASAN, K. R. 1995 On the universality of the Kolmogorov constant. *Phys. Fluids* **7** (1), 2778–2784.
- SWEARINGEN, J. D. & BLACKWELDER, R. F. 1987 The growth and breakdown of streamwise vortices in the presence of a wall. *J. Fluid Mech.* **182**, 255–290.
- SZABÓ, B., DÜSTER, A. & RANK, E. 2004 *The p-Version of the Finite Element Method*. Wiley.
- TENNEKES, H. & LUMLEY, J. L. 1972 *A First Course in Turbulence*. MIT Press.
- DU TOIT, C. G. & SLEATH, J. F. A. 1981 Velocity measurements close to rippled beds in oscillatory flow. *J. Fluid Mech.* **112**, 71–96.
- VAN ATTA, C. W. & ANTONIA, R. A. 1980 Reynolds number dependence of skewness and flatness factors of turbulent velocity derivatives. *Phys. Fluids* **23** (2), 252–257.
- VITTORI, G. & VERZICCO, R. 1998 Direct simulation of transition in an oscillatory boundary layer. *J. Fluid Mech.* **371**, 207–232.
- VOS, P. E. J., ESKILSSON, C., BOLIS, A., CHUN, S., KIRBY, R. M. & SHERWIN, S. J. 2011 A generic framework for time-stepping partial differential equations (PDEs): general linear methods, object-oriented implementation and application to fluid problems. *Intl J. Comput. Fluid Dyn.* **25** (3), 107–125.
- WEISS, J. 1991 The dynamics of enstrophy transfer in two-dimensional hydrodynamics. *Physica D* **48** (2–3), 273–294.
- VAN DER WERF, J. J., DOUCETTE, J. S., O'DONOGHUE, T. & RIBBERINK, J. S. 2007 Detailed measurements of velocities and suspended sand concentrations over full-scale ripples in regular oscillatory flow. *J. Geophys. Res.* **112**, F02012.
- VAN DER WERF, J. J., RIBBERINK, J. S., O'DONOGHUE, T. & DOUCETTE, J. S. 2006 Modelling and measurement of sand transport processes over full-scale ripples in oscillatory flow. *Coast. Engng* **53** (8), 657–673.
- WILLIAMSON, C. H. K. 1996 Vortex dynamics in the cylinder wake. *Annu. Rev. Fluid Mech.* **28** (1), 477–539.
- YUAN, J., DONGXU, W. & MADSEN, O. S. 2017 A laser-based bottom profiler system for measuring net sediment transport rate in an oscillatory water tunnel. In *Proceedings of Coastal Dynamics 2017*, pp. 1495–1505.
- ZEDLER, E. A. & STREET, R. L. 2006 Sediment transport over ripples in oscillatory flow. *J. Hydraul. Engng* **132** (2), 180–193.